Micromechanics-based thermoelastic model for functionally graded particulate materials with particle interactions

H.M. Yin[a],*, G.H. Paulino[a], W.G. Buttlar[a], L.Z. Sun[b]

[a]Department of Civil and Environmental Engineering, Newmark Laboratory, 205 North Mathews Avenue, University of Illinois at Urbana-Champaign, Urbana, IL 61801, USA
[b]Department of Civil and Environmental Engineering, 4139 Engineering Gateway, University of California, Irvine, CA 92697, USA

Abstract

Thermoelastic behavior of functionally graded particulate materials is investigated with a micromechanical approach. Based on a special representative volume element constructed to represent the graded microstructure of a macroscopic material point, the relation between the averaged strains of the particle and matrix phases is derived with pair-wise particle interactions, and a set of governing equations for the thermoelastic behavior of functionally graded materials is presented. The effective coefficient of thermal expansion at a material point is solved through the overall averaged strain of two phases induced by temperature change under the stress-free condition, and is shown to exhibit a weak anisotropy due to the particle interactions within the graded microstructure. When the material gradient is eliminated, the proposed model predicts the effective coefficient of thermal expansion for uniform composites as expected. If the particle interactions are disregarded, the proposed model recovers the Kerner model. The proposed semi-analytical scheme is consistent and general, and can handle any thermal loading variation. As examples, the thermal stress distributions of graded thermal barrier coatings are solved for two types of thermal loading: uniform temperature change and steady-state heat conduction in the gradation direction.
© 2006 Elsevier Ltd. All rights reserved.

*Corresponding author. Tel.: +1 217 333 0047; fax: +1 217 333 1924.
E-mail address: huiming@uiuc.edu (H.M. Yin).

1. Introduction

Functionally graded materials (FGMs) are characterized by continuous variation of the volume fraction of the constituents (Miyamoto et al., 1999). In recent years, FGMs have been manufactured for various multifunctional tasks (Suresh and Mortensen, 1998; Paulino, 2004). For instance, in ceramic/metal two-phase FGMs, a continuous trade-off between the fracture toughness and high thermal-conductivity of metals is utilized with the high hardness and low thermal conductivity of ceramics. In heat and impact protection applications, the material multifunctionality consists of the ability to provide structural support by virtue of the metallic portions of FGMs, and the simultaneous ability of the same material system to provide the required thermal or impact resistance by virtue of the ceramic portions of FGMs. Due to the gradually varying microstructure, the overall thermomechanical response of the material system continuously changes in the gradation direction and, thus, thermal stresses may be reduced as compared to corresponding two-layer or bimaterial systems (Paulino et al., 2003).

Investigation of effective thermomechanical properties of FGMs has attracted a significant amount of attention in recent years. Kesler et al. (1998), Ishibashi et al. (2000), and Khor and Gu (2000) have employed different approaches to obtain the effective coefficients of thermal expansion (CTE) and thermal stress distribution of FGMs in the gradation direction. Finite element models have been used to simulate thermomechanical response and to analyze experimental results (Dao et al., 1997; Reiter and Dvorak, 1998; Neubrand et al., 2002; Agrawal et al., 2003). Because FGMs generally have a complex microstructure and the accuracy of numerical simulations depends on the quality of meshing (e.g. discretization aspects), it is not straightforward to extend these results to general cases.

Effective medium theory has been successfully developed to predict the effective elastic constants and CTEs for homogeneous composites. Although FGMs have quite different microstructure from homogenous composites, the Mori–Tanaka (Mori and Tanaka, 1973) and self-consistent (Hill, 1965; Budiansky, 1965) models have been directly employed to estimate the effective moduli and CTEs for FGMs as seen in Reiter and Dvorak (1998), Vel and Batra (2003), and Kim and Paulino (2003) among others. Buryachenko and Rammerstorfer (2001) and Tsukamoto (2003) approximated the continuous volume fraction distribution function of an FGM with a step function. As a result, the FGM was transferred into a multi-layer system. However, none of these approaches directly considered the continuous material gradient nature and local particle interaction of FGMs at the microscopic scale.

Some studies have suggested the need to consider the effect of a continuous volume fraction gradient on the effective properties of an FGM. For instance, Zuiker and Dvorak (1994) extended the Mori–Tanaka method to linearly varying fields and investigated the relations of the averaged stress versus strain relation, and of the stress-gradient versus strain-gradient, which was shown to be dependent on the size of the representative volume element (RVE). By definition, a RVE in a continuum body is a material volume that statistically represents the neighborhood of a material point (Nemat-Nasser and Hori, 1999). Aboudi et al. (1999) developed a higher-order cell theory based on volumetric averaging of the mechanical fields and numerically studied the micro–macro-structural coupling effect in the effective thermomechanical behavior of FGMs.

The purpose of this work is to investigate the effective thermoelastic behavior of FGMs considering local particle interactions and particle distributions. An FGM, illustrated in Fig. 1(a), microscopically contains a particle–matrix zone with dispersed particles filled in a continuous matrix, followed by a skeletal transition zone in which the particle and matrix phases cannot be well defined because the two phases are interpenetrated into one other as a connected network. The transition zone is followed by another particle–matrix zone with interchanged phases of particle and matrix (Yin et al., 2004). Macroscopically, the FGM is observed as a homogeneous material with varying effective material properties along the gradation direction in a continuous and differentiable fashion (Eischen, 1987). To solve the overall behavior based on the microstructure, a graded RVE is constructed to represent the microstructure at the neighborhood of a material point in the particle–matrix zones. By integrating the pair-wise particle interactions from all other particles over the RVE, the relation between the particle and matrix averaged strains for FGMs subjected to thermal and mechanical loading is obtained. Then, a set of governing equations are provided for the thermoelastic behavior of FGMs.

Effective CTEs of composite materials is generally defined through the overall averaged strain of a material point induced by temperature change under the stress-free condition (Kingery et al., 1976). Using the governing equations of FGMs, the averaged thermal strain distribution in the gradation direction is solved. In the transition zone, a transition function (Reiter and Dvorak, 1998; Yin et al., 2004) is introduced to make the averaged strain fields continuous and differentiable in the gradation direction. From the relation between averaged thermal strain and temperature change, the effective CTE distribution is obtained. The effective CTEs are weakly anisotropic due to the particle interaction and graded microstructure. When the material gradient is reduced to zero, the proposed model can also predict the effective CTEs and thermal stresses of both phases for uniform
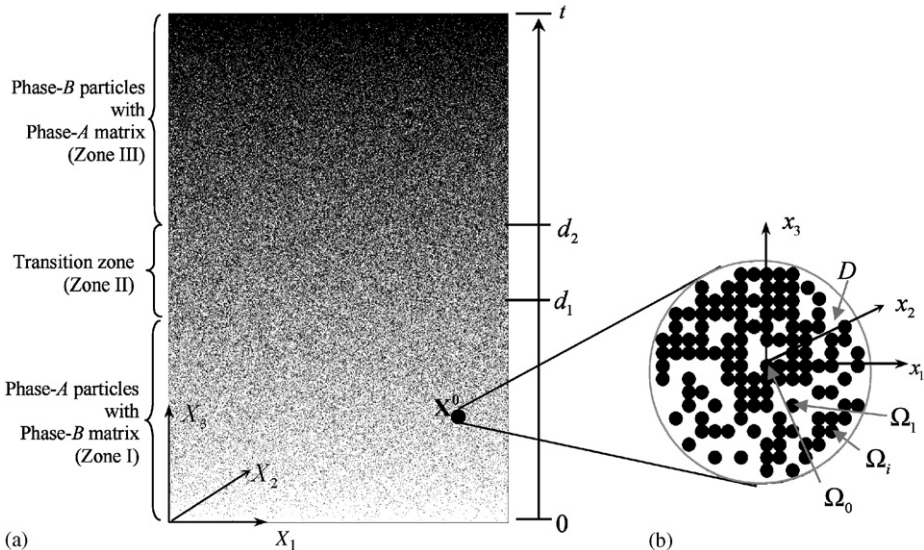
Fig. 1. Schematic illustration of a two-phase FGM graded along the X_3 direction: (a) microstructure including A and B phases and three zones, and (b) RVE of the neighborhood of the material point X^0. The global coordinate system is denoted (X_1, X_2, X_3) and the local coordinate system is denoted (x_1, x_2, x_3).

composites. Further, disregarding the particle interactions, the effective CTEs are predicted by means of an explicit form, which recovers the former Kerner model (1956).

The proposed method is also used to calculate the thermal stress distribution of FGMs for different boundary conditions and loading conditions. For a graded thermal barrier coating (TBC) deposited onto a uniform substrate, the horizontal deformation is constrained by the substrate and the vertical deformation is free. To simulate the deposition and application of TBCs, two types of loading conditions are considered: the uniform temperature change and the steady-state temperature field for the upper and lower surfaces of the FGM with different temperatures. For the latter case, the temperature field in TBCs is first solved. The averaged strain distribution for each phase of the FGM is then derived, and, finally, the thermal stress distribution is obtained.

The remainder of this paper is organized as follows. Section 2 defines the pairwise interaction for two interacting particles filled in the infinite domain subject to a far-field stress and uniform temperature change, and uses it to obtain the governing equations for thermoelastic behavior of FGMs. Section 3 studies the effective CTE distribution in FGMs. When the material gradient is null, the proposed model predicts the effective CTE for uniform composites. Section 4 simulates the thermal stress distributions in graded TBCs under uniform temperature change and steady-state heat conduction. Concluding remarks are given in Section 5.

2. Micromechanical analysis of the RVE

Consider a particulate FGM (Fig. 1(a)) containing two phases A and B with isotropic elastic tensors $\mathbf{C}^A$ and $\mathbf{C}^B$ and isotropic CTEs α^A and α^B, respectively. The overall grading length of the FGM is t (thickness). The global coordinate system of the FGM is denoted by (X_1, X_2, X_3) with X_3 being the continuous gradation direction. Three material zones exist in the gradation direction: zone I $(0 \leqslant X_3 \leqslant d_1)$ including discrete particles of phase A with the continuous matrix of phase B; zone III $(d_2 \leqslant X_3 \leqslant t)$ including discrete particles of phase B with the continuous matrix of phase A, and; special transition zone II $(d_1 \leqslant X_3 \leqslant d_2)$ including interpenetrating phases (Reiter and Dvorak, 1998; Torquato, 2002). Here the boundaries of the transition zone are denoted by d_1 and d_2, which could be obtained from microstructure characterization (Bao and Cai, 1997). Typically, in each graded thin layer ($X_1 - X_2$ plane), micro-particles are uniformly dispersed with a two-dimensionally random setting so that the material layer is statistically homogeneous. Although these micro-particles, whose sizes are much smaller than the thickness of the FGM, cannot be observed at the macroscopic scale, the volume fraction of phase A or B varies gradually in the X_3 direction.

For any macroscopic material point, the effective material behavior depends upon the microstructural features in the local neighborhood of the point. For convenience, a material point $\mathbf{X}^0$ is arbitrarily chosen in the range of $0 \leqslant X_3 \leqslant d_1$ (zone I) (Fig. 1(a)). A graded RVE is introduced to represent the microstructure in the neighborhood of the material point (Fig. 1(b)). The RVE contains a number of micro-particles of the phase A embedded in a continuous matrix of the phase B, and the overall volume fraction of particle phase A and its gradient should be consistent with the macroscopic counterparts $\phi(X_3^0)$ and $\mathrm{d}\phi/\mathrm{d}X_3|_{X_3=X^0}$. Here, ϕ denotes the volume fraction of phase A, and thus, the volume fraction of phase B is $1-\phi$. The local coordinate system (x_1, x_2, and x_3) is constructed with the origin corresponding to $\mathbf{X}^0$ to represent the microstructure. All micro-particles are assumed to be spherical with identical radius $a(a \ll t)$. The entire RVE

domain is denoted as D and the ith micro-particle's ($i = 1, 2, 3,\ldots, \infty$) domain is denoted as Ω_i, which is centered at $\mathbf{x}^i$. For ease of formulation, a particle centered at the origin is assumed and denoted as Ω_0.

Originally, the FGM is free-standing with no initial stress or strain at any point. When it is subjected to a uniform thermomechanical loading, an overall deformation at the material point X^0 can be observed at the macroscopic scale. This deformation is obtained by the averaged deformation of the particles and matrix in the corresponding $X_1 - X_2$ plane. At the microscopic scale, the discrete particles are constrained by the matrix, and the occurrence of a particle has an interaction on the elastic fields of neighboring particles. The relation between particle and matrix deformations depends on the constituents and microstructure of the RVE. In the following, the thermoelastic interaction between particles in the RVE under a thermomechanical loading is first investigated; the relation between the particle and matrix strains of the RVE with particle interactions is then derived, and finally; the governing equations for thermomechanical behavior of FGMs are provided.

2.1. Pair-wise thermoelastic interaction in the RVE

To analytically solve the interaction between particles, the RVE including only the particle Ω_0 is first considered. When this RVE is subjected to a uniform temperature change and a uniform stress on the boundary, the local elastic field in the neighborhood of the particle is distorted due to the material mismatch in both the stiffness and CTE. Using Eshelby's equivalent inclusion method (Eshelby, 1957, 1959), the material elastic mismatch is simulated by introducing an eigenstrain on the particle, and then the problem is reduced to a homogeneous domain with the matrix material subjected to the uniform thermomechanical loading along with the particle elastic and thermal equivalent eigenstrains in the particle domain.

Based on the Eshelby's equivalent inclusion method, the local strain field at a certain point $\mathbf{x}$ for the phase A particle embedded in the phase B matrix under the external far-field stress $\boldsymbol{\sigma}^0$ and the temperature change T can be written as

$$\boldsymbol{\varepsilon}(\mathbf{x}) = \boldsymbol{\varepsilon}^0 + \boldsymbol{\varepsilon}'(\mathbf{x}), \tag{1}$$

where

$$\boldsymbol{\varepsilon}^0 = \left(\mathbf{C}^B\right)^{-1} : \boldsymbol{\sigma}^0 + \alpha^B T \boldsymbol{\delta}, \tag{2}$$

denotes the uniform strain caused by the thermomechanical loading, in which $\boldsymbol{\delta}$ is the second rank unit tensor or the Kronecker Delta tensor, and the disturbed strain $\boldsymbol{\varepsilon}'$ due to the material mismatch between the particle and the matrix reads:

$$\boldsymbol{\varepsilon}'(\mathbf{x}) = -\int_{\Omega_0} \boldsymbol{\Gamma}(\mathbf{x} - \mathbf{x}') \cdot \mathbf{C}^B : \left[\boldsymbol{\varepsilon}^*(\mathbf{x}') + \boldsymbol{\varepsilon}^{\mathrm{T}}\right] \mathrm{d}\mathbf{x}', \tag{3}$$

in which the symbols " $\cdot$ "and ":" indicate the tensor contraction between two fourth-rank tensors and between fourth-rank and second-rank tensors, respectively. In addition, $\boldsymbol{\varepsilon}^*$ denotes the elastic equivalent eigenstrain (to be solved later) and $\boldsymbol{\varepsilon}^{\mathrm{T}}$ is the thermal equivalent eigenstrain written as

$$\boldsymbol{\varepsilon}^{\mathrm{T}} = \left(\alpha^A - \alpha^B\right) T \boldsymbol{\delta}. \tag{4}$$

Compared with the size of the RVE, the particle is sufficiently small to be considered as embedded in an infinite domain. Thus, the modified two-point Green function $\boldsymbol{\Gamma}$ (Kröner,

1990) can be written as

$$\Gamma_{ijkl}(\mathbf{x} - \mathbf{x}') = \frac{1}{16\pi\mu^B(1 - v^B)}\left[-\psi_{,ijkl} + (1 - v^B)\left(\delta_{ik}\varphi_{,lj} + \delta_{il}\varphi_{,jk} + \delta_{jk}\varphi_{,il} + \delta_{jl}\varphi_{,ik}\right)\right]$$
(5)

with $\psi = |\mathbf{x} - \mathbf{x}'|$, $\varphi = 1/|\mathbf{x} - \mathbf{x}'|$, and μ^B and v^B being the shear modulus and the Poisson ratio of the matrix, respectively. Here, $\mathbf{\Gamma}(\mathbf{x} - \mathbf{x}')$ describes the response strain at an arbitrary point $\mathbf{x}$ due to the unit source eigenstrain at a certain point $\mathbf{x}'$. Because eigenstrain only exists in the particle domain Ω_0, the disturbed strain is written in an integral form as shown in Eq. (3).

From the stress equivalent formulation in the spherical particle domain,

$$\mathbf{C}^A : \left[\mathbf{\varepsilon}^0 + \mathbf{\varepsilon}'(\mathbf{x}) - \alpha^A T\mathbf{\delta}\right] = \mathbf{C}^B : \left[\mathbf{\varepsilon}^0 + \mathbf{\varepsilon}'(\mathbf{x}) - \mathbf{\varepsilon}^*(\mathbf{x}) - \alpha^A T\mathbf{\delta}\right],$$
(6)

the equivalent eigenstrain $\mathbf{\varepsilon}^*$ is derived as

$$\mathbf{\varepsilon}^* = \left(\mathbf{C}^B\right)^{-1} \cdot \left(\mathbf{P}^0 - \Delta\mathbf{C}^{-1}\right)^{-1} : \left(\mathbf{\varepsilon}^0 - \alpha^A T\mathbf{\delta} - \mathbf{P}^0 \cdot \mathbf{C}^B : \mathbf{\varepsilon}^T\right),$$
(7)

where the elasticity mismatch tensor $\Delta\mathbf{C} = \mathbf{C}^A - \mathbf{C}^B$, and

$$P^0_{ijkl} = \frac{\delta_{ij}\delta_{kl} - \left(4 - 5v^B\right)\left(\delta_{ik}\delta_{jl} + \delta_{il}\delta_{jk}\right)}{30\mu^B(1 - v^B)}.$$
(8)

The combination of Eqs. (1), (3) and (7) yields the local strain field due to a single particle Ω_0 embedded in the matrix. In particular, the strain field in the spherical particle domain Ω_0 is shown to be uniform as

$$\mathbf{\varepsilon}_\Omega = \alpha^A T\mathbf{\delta} + \left(\mathbf{I} - \mathbf{P}^0 \cdot \Delta\mathbf{C}\right)^{-1} : \left(\mathbf{\varepsilon}^0 - \alpha^A T\mathbf{\delta} - \mathbf{P}^0 \cdot \mathbf{C}^B : \mathbf{\varepsilon}^T\right),$$
(9)

where the standard fourth rank unit tensor is $I_{ijkl} = \left(\delta_{ik}\delta_{jl} + \delta_{il}\delta_{jk}\right)/2$.

If another identical particle Ω_1 centered at $\mathbf{x}^1$ is added in the RVE, the strain field in the particle domain is no longer uniform. Using the equivalent inclusion method, Moschovidis and Mura (1975) solved the elastic problem of two particles embedded in the infinite domain under uniform far field strain. In a similar fashion, the current thermoelastic problem can be solved (see Appendix A). Then, the averaged strain in the first spherical particle domain Ω_0 can be derived by integrating the local strain field over the particle as

$$\bar{\mathbf{\varepsilon}}_\Omega = \alpha^A T\mathbf{\delta} + \left\{\mathbf{I} - \left[\mathbf{P}^0 + \mathbf{P}\left(\mathbf{x}^1\right)\right] \cdot \Delta\mathbf{C}\right\}^{-1} : \left\{\mathbf{\varepsilon}^0 - \alpha^A T\mathbf{\delta}\right.$$
$$\left. - \left[\mathbf{P}^0 + \mathbf{P}\left(\mathbf{x}^1\right)\right] \cdot \mathbf{C}^B : \mathbf{\varepsilon}^T\right\} + O\left(\rho^8\right),$$
(10)

where $\rho = a/|\mathbf{x}^1|$ and the precision reaches the order of $O(\rho^8)$. Because $\rho \leqslant 0.5$, this precision is fairly high. In addition, the fourth-rank tensor $\mathbf{P}$ reads:

$$P_{ijkl}\left(\mathbf{x}^1\right) = \int_{\Omega_1} \Gamma_{ijkl}(\mathbf{x}') \, d\mathbf{x}'$$
$$= \frac{\rho^3}{60\mu^B(1 - v^B)}\begin{bmatrix} \left(5 - 3\rho^2\right)\delta_{ij}\delta_{kl} - \left(5 - 10v^B + 3\rho^2\right)\left(\delta_{ik}\delta_{jl} + \delta_{il}\delta_{jk}\right) \\ +15\left(5 - 7\rho^2\right)n_in_jn_kn_l - 15\left(1 - \rho^2\right)\left(\delta_{ij}n_kn_l + \delta_{kl}n_in_j\right) \\ -15\left(v^B - \rho^2\right)\left(\delta_{ik}n_jn_l + \delta_{jk}n_in_l + \delta_{il}n_jn_k + \delta_{jl}n_in_k\right) \end{bmatrix}$$
(11)

with $\mathbf{n} = \mathbf{x}^1/|\mathbf{x}^1|$. Comparison of Eqs. (9) and (10) shows the additional particle provides an interaction term on the averaged strain of the first particle as

$$\mathbf{d}(\mathbf{0}, \mathbf{x}^1) = \Delta\mathbf{C}^{-1} \cdot \mathbf{L}(\mathbf{0}, \mathbf{x}^1) : (\boldsymbol{\varepsilon}^0 - \alpha^A T\boldsymbol{\delta} - \Delta\mathbf{C}^{-1} \cdot \mathbf{C}^B : \boldsymbol{\varepsilon}^{\mathrm{T}}) + O(\rho^8), \tag{12}$$

where the pair-wise interaction tensor is

$$\mathbf{L}(\mathbf{0}, \mathbf{x}^1) = [\Delta\mathbf{C}^{-1} - \mathbf{P}^0 - \mathbf{P}(\mathbf{x}^1)]^{-1} - (\Delta\mathbf{C}^{-1} - \mathbf{P}^0)^{-1}. \tag{13}$$

It is noted that the pair-wise interaction term in Eq. (12) denotes the contribution of the occurrence of the second particle to the averaged strain of the first particle. The magnitude of the interaction not only depends on the nature of the imposed thermomechanical loading, but also relies on the distance between particles. As the spacing between two particles becomes smaller, the disturbed strain becomes larger and thus the interaction is stronger. Notice that the tensor $\mathbf{P}$ in Eq. (11) contains some terms of the vector $\mathbf{n}$, and the mathematical inverse operation of the fourth-rank tensor that appears in Eqs. (10) and (13) can be found in Ju and Chen (1994). Thus, the fourth-rank pair-wise interaction tensor $\mathbf{L}$ can be explicitly derived as given in Appendix B. Numerically, if the vector $\mathbf{n}$ is known, the components of the tensor $\mathbf{P}$ can be solved and the inverse can be calculated through the matrix operations of the six-dimensional representation of a fourth-rank tensor (Cowin and Mehrabadi, 1995).

2.2. Particle averaged strain with particle interactions in the RVE of FGMs

When an FGM is subjected to thermomechanical loading, the averaged strains of the particles and the matrix vary in the gradation direction. For an arbitrarily chosen X_3^0 in Fig. 1(a), its neighboring microstructure is represented as the RVE in Fig. 1(b). Because the particle size is much smaller than the macroscopic size (such as the thickness t of FGMs), the RVE may contain many particles. Drugan and Willis (1996) and Drugan (2000, 2003) have demonstrated that, when the size of a RVE is larger than a specific value, the modeling result is no longer sensitive to the size of the RVE. Therefore, for modeling convenience, it is assumed that the RVE includes an infinite number of particles and that the volume of the RVE is not bounded. In the central region of the RVE, the particle distribution is consistent with the global volume fraction distribution. Without any loss of generality, the averaged strain of the central particle of the RVE is used to represent the particle averaged strain at X_3^0 in the gradation direction.

At the microscopic scale, particles are randomly dispersed in the matrix. It is not possible to obtain an exact solution for the local strain field as in the previous subsection due to the uncertainty of the particle distribution. However, the averaged strain of the central particle can be estimated in the following way:

- when there is only one particle, the averaged strain is obtained from the single particle solution, as given by Eq. (9);
- as more particles are added into the RVE, each additional particle will produce an interaction on the central particle as given by Eq. (12).

Therefore, the averaged strain in the central particle Ω_0 can be written in two parts: a single particle solution (for the central particle embedded in the RVE) and pair-wise

interaction terms for all other particles:

$$\langle\boldsymbol{\varepsilon}\rangle^A(\mathbf{0}) = \alpha^A T\boldsymbol{\delta} + (\mathbf{I} - \mathbf{P}^0 \cdot \Delta\mathbf{C})^{-1} : [\langle\boldsymbol{\varepsilon}\rangle^B(0) - \alpha^A T\boldsymbol{\delta} - \mathbf{P}^0 \cdot \mathbf{C}^B : \boldsymbol{\varepsilon}^{\mathrm{T}}] + \sum_{i=1}^{\infty}\mathbf{d}(\mathbf{0},\mathbf{x}^i),$$

(14)

where the angular brackets $\langle\bullet\rangle^A$ and $\langle\bullet\rangle^B$ denote the volume averages over the phases A and B in the X_1-X_2 layer, respectively. It is noted that, due to the existence of so many distributed particles, the matrix averaged strain is no longer solely decided by the external thermomechanical loading as in Eq. (2). It is also affected by the particle distribution. Because the central particle is constrained and loaded through the surrounding matrix, based on the mean-field approximation (Yin et al, 2005; Torquato, 2002), the uniform thermomechanical strain $\boldsymbol{\varepsilon}^0$ of Eq. (9) is replaced by the matrix averaged strain $\langle\boldsymbol{\varepsilon}\rangle^B$ in Eq. (14).

Because the matrix averaged strain varies in the gradation direction, from Eq. (12), the particle interaction term is written as

$$\mathbf{d}(\mathbf{0},\mathbf{x}^i) = \Delta\mathbf{C}^{-1} \cdot \mathbf{L}(\mathbf{0},\mathbf{x}^i) : [\langle\boldsymbol{\varepsilon}\rangle^B(x_3^i) - \alpha^A T\boldsymbol{\delta} - \Delta\mathbf{C}^{-1} \cdot \mathbf{C}^B : \boldsymbol{\varepsilon}^{\mathrm{T}}] + O(\rho^8),$$

(15)

in which $\langle\boldsymbol{\varepsilon}\rangle^B(x_3^i)$ is the averaged matrix strain in the x_3^ith layer. Because all particles are statistically distributed in a random fashion, the total particle interactions can be obtained by integrating the pair-wise interaction of Eq. (15) over all possible particle positions as:

$$\langle\mathbf{d}\rangle(\mathbf{0}) = \sum_{i=1}^{\infty}\mathbf{d}(\mathbf{0},\mathbf{x}^i) = \int_D P(\mathbf{x}|\mathbf{0})\mathbf{d}(\mathbf{0},\mathbf{x})\,\mathrm{d}\mathbf{x},$$

(16)

where $P(\mathbf{x}|\mathbf{0})$ is the conditional number density function used to locate a particle centered at $\mathbf{x}$ when the first particle is located at $\mathbf{0}$. Following our recent work (Yin et al., 2004), the particle number density function is introduced as

$$P(\mathbf{x}|\mathbf{0}) = \frac{3g(x)}{4\pi a^3}[\phi(X_3^0) + \mathrm{e}^{-x/\delta}\phi_{,3}(X_3^0)x_3],$$

(17)

where $g(x)$ with $x = |\mathbf{x}|$ denotes the Percus–Yevick radial distribution function (Percus and Yevick, 1958; Tsang et al., 2001) and δ represents the attenuating rate of the gradation of the particle volume fraction in the far field. Given that the maximum volume fraction of particles in the RVE should not be greater than the maximum volume fraction in the particle–matrix zone and that the minimum volume fraction is zero, we can impose:

$$\delta = \frac{e}{\phi_{,3}(X_3^0)}\min(\phi, \phi^c - \phi),$$

(18)

where ϕ^c denotes the maximum volume fraction in the particle–matrix zone. Because the averaged matrix strain $\langle\boldsymbol{\varepsilon}\rangle^B$ continuously and differentially changes along with coordinate x_3, it can be written in terms of a Taylor expansion, i.e.,

$$\langle\boldsymbol{\varepsilon}\rangle^B(x_3) = \langle\boldsymbol{\varepsilon}\rangle^B(0) + \langle\boldsymbol{\varepsilon}\rangle_{,3}^B(x_3)x_3 + \cdots.$$

(19)

Truncating $\langle\boldsymbol{\varepsilon}\rangle^B(x_3)$ to a linear expression in terms of x_3 and disregarding the higher-order terms $O(\rho^8)$ in Eq. (15), one can analytically integrate the interactions in

Eq. (16) as:

$$\langle \mathbf{d} \rangle(0) = \phi\left(X_3^0\right)\Delta \mathbf{C}^{-1} \cdot \mathbf{D}(0) : \left[\langle \boldsymbol{\varepsilon} \rangle^B(0) - \alpha^A T \boldsymbol{\delta} - \Delta \mathbf{C}^{-1} \cdot \mathbf{C}^B : \boldsymbol{\varepsilon}^{\mathrm{T}}\right]$$
$$+ \phi_{,3}\left(X_3^0\right)\Delta \mathbf{C}^{-1} \cdot \mathbf{F}(0) : \langle \boldsymbol{\varepsilon} \rangle_{,3}^B(0), \tag{20}$$

where

$$\mathbf{D}(0) = \int_{2a}^{\infty} \frac{g(x)}{5a\rho^2} \left[(15c_1 + 10c_3 + c_5)\delta_{ij}\delta_{kl} + (15c_2 + 10c_4 + c_5)\left(\delta_{ik}\delta_{jl} + \delta_{il}\delta_{jk}\right)\right] \mathrm{d}x \tag{21}$$

and

$$\mathbf{F}(0) = \int_{2a}^{\infty} \mathrm{e}^{-(x/\delta)} \frac{g(x)a}{35\rho^4} \left\{ \begin{array}{c} [35c_1 + 14c_3 + c_5 + 2(7c_3 + c_5)(\delta_{I3} + \delta_{K3})]\delta_{ij}\delta_{kl} + \\ [35c_2 + 14c_4 + c_5 + 2(7c_4 + c_5)(\delta_{I3} + \delta_{J3})]\left(\delta_{ik}\delta_{jl} + \delta_{il}\delta_{jk}\right) \end{array} \right\} \mathrm{d}x. \tag{22}$$

Here, the definitions of c_i ($i = 1, 2,\ldots,5$) and the derivations of the tensors $\mathbf{D}$ and $\mathbf{F}$ are given in Appendix B. It is noted that Mura's (1987) tensorial indicial notation is followed in the above equation; i.e., uppercase indices have the same representation as the corresponding lowercase ones, but are not summed. Due to the anisotropy of the tensor $\mathbf{F}$, the effective material behavior is also anisotropic, which is illustrated later.

Substituting Eq. (20) into Eq. (14), and recognizing that the origin of the local coordinates in the RVE corresponds to the global coordinate point $\mathbf{X}^0$ of the FGM, one can obtain the averaged particle strain tensor in terms of the arbitrary material point X_3

$$\langle \boldsymbol{\varepsilon} \rangle^A(X_3) = \alpha^A T \boldsymbol{\delta} + (\mathbf{I} - \mathbf{P}_0 \cdot \Delta \mathbf{C})^{-1} : \left[\langle \boldsymbol{\varepsilon} \rangle^B(X_3) - \alpha^A T \boldsymbol{\delta} - \mathbf{P}_0 \cdot \mathbf{C}^B : \boldsymbol{\varepsilon}^{\mathrm{T}}\right]$$
$$+ \phi(X_3)\Delta \mathbf{C}^{-1} \cdot \mathbf{D}(X_3) : \left[\langle \boldsymbol{\varepsilon} \rangle^B(X_3) - \alpha^A T \boldsymbol{\delta} - \Delta \mathbf{C}^{-1} \cdot \mathbf{C}^B : \boldsymbol{\varepsilon}^{\mathrm{T}}\right].$$
$$+ \phi_{,3}(X_3)\Delta \mathbf{C}^{-1} \cdot \mathbf{F}(X_3) : \langle \boldsymbol{\varepsilon} \rangle_{,3}^B(X_3) \tag{23}$$

This is the governing ordinary differential equation for the present problem.

2.3. Governing equations for overall material behavior

When the FGM is subjected to a thermomechanical loading, the overall material behavior is represented by the overall averaged stress and strain distributions at the macroscopic scale, which change in the gradation direction. The averaged stress and strain in the $X_1 - X_2$ layer are defined as the volume average of the stress and strain on the two phases, and are expressed as

$$\langle \boldsymbol{\sigma} \rangle(X_3) = \phi(X_3)\left[\langle \boldsymbol{\sigma} \rangle^A(X_3)\right] + [1 - \phi(X_3)]\left[\langle \boldsymbol{\sigma} \rangle^B(X_3)\right], \tag{24}$$

$$\langle \boldsymbol{\varepsilon} \rangle(X_3) = \phi(X_3)\langle \boldsymbol{\varepsilon} \rangle^A(X_3) + [1 - \phi(X_3)]\langle \boldsymbol{\varepsilon} \rangle^B(X_3), \tag{25}$$

where the angular bracket $\langle \bullet \rangle$ denotes the volume average over the entire FGM domain of the $X_1 - X_2$ layer. For each phase, the averaged stress is related to the averaged strain as:

$$\langle \boldsymbol{\sigma} \rangle^A(X_3) = \mathbf{C}^A : \left(\langle \boldsymbol{\varepsilon} \rangle^A(X_3) - \alpha^A T \boldsymbol{\delta}\right), \tag{26}$$

$$\langle \boldsymbol{\sigma} \rangle^B(X_3) = \mathbf{C}^B : \left(\langle \boldsymbol{\varepsilon} \rangle^B(X_3) - \alpha^B T \boldsymbol{\delta}\right). \tag{27}$$

In addition, the particle averaged strain is related to the matrix averaged strain by Eq. (23). Eqs. (23)–(27) form the governing equations for the thermomechanical behavior of FGMs. Here six tensor variables are included in the five equations, which are the averaged stress and strain for phases A and B, and for the overall material point. If the overall averaged stress or strain distribution is given, all other variables can be calculated through these governing equations. In the following two sections, two specific cases are considered. First, letting the overall averaged stress be zero for each material point, the overall averaged strain is solved and the effective CTE distribution in the gradation direction is obtained; then, considering the overall averaged strain of FGMs constrained by stiff and thick substrates, the thermal stress distribution in graded TBCs is calculated.

It is noted that Eq. (23) is derived for zone I with the phase A as particles and the phase B as matrix. In the other particle–matrix zone, the relation between the particle and matrix averaged strains can be similarly obtained by interchanging the roles of phases A and B. In the transition zone, a transition function will be introduced to simulate the microstructural transition between two particle–matrix zones, which is discussed Section 3.

3. Effective CTE distribution

The effective CTE for a composite material is generally measured as the overall averaged strain at a unit temperature change under the stress-free condition (Kingery et al., 1976). In FGMs, the effective CTE, which is an intrinsic physical quantity for a material point, continuously changes in the gradation direction. Consider a free-standing FGM under a uniform temperature change. For a constant or linear effective CTE distribution in the gradation direction, the thermally induced strain is uniform or linear, respectively, which satisfies compatibility, so that no thermal stress is induced. However, the effective CTE distribution in general FGMs may be nonlinear. Due to loss of compatibility of the thermally induced strain, which is discussed in detail later, thermal stress must be present to make the total strain compatible. Therefore, the effective CTE may not be directly observed from the total strain distribution in the gradation direction in a free-standing FGM under uniform temperature change. For a certain material point, the effective CTE can be experimentally measured within individual thin slices cut perpendicular to the gradation direction (Ishibashi et al., 2000), in which the thermal stress is very close to zero in the thin slices. Herein, to analytically obtain the effective CTE at the material point, the overall averaged stress is assumed to be zero. From the relation between the overall averaged strain and the temperature change, the effective CTE can be obtained.

3.1. Formulation of effective CTE

For an FGM under uniform temperature change, although the averaged stress of a material point is set to be zero, thermal stress will be induced due to the CTE mismatch between the particles and the matrix at the microscopic scale. Therefore, the averaged stresses of both the particle and the matrix phases are not zero. From Eq. (24), we obtain

$$\phi(X_3)\big[\langle\boldsymbol{\sigma}\rangle^A(X_3)\big] + [1 - \phi(X_3)]\big[\langle\boldsymbol{\sigma}\rangle^B(X_3)\big] = \mathbf{0}. \tag{28}$$

With the combination of Eqs. (23), (24), and (26)–(28), the averaged particle strain tensor $\langle\boldsymbol{\varepsilon}\rangle^A(X_3)$ and the averaged matrix strain tensor $\langle\boldsymbol{\varepsilon}\rangle^B(X_3)$ along the FGM gradation direction X_3 can be solved. Since Eq. (23) represents a set of ordinary differential

equations, the appropriate boundary condition is needed. In the particle–matrix zone with $0 \leqslant X_3 \leqslant d_1$, the boundary at $X_3 = 0$ corresponds to the 100% matrix material (i.e., $\phi(0) = 0$). Thus, the corresponding boundary conditions can be proposed as

$$\langle \boldsymbol{\varepsilon} \rangle^B(0) = \alpha^B T \boldsymbol{\delta}. \tag{29}$$

In some specific FGMs (Aboudi et al., 1999; Neubrand et al., 2002), the volume fraction range of one material phase may not vary across the entire possible range, i.e., 0–1. For example, the volume fraction of a given phase may not reach 100%. In such instances, the boundary condition presented in Eq. (29) is not applicable. However, the modified boundary condition of $\langle \boldsymbol{\varepsilon} \rangle^B(0)$ can be derived with the aid of an appropriate uniform composite model (as seen in Eq. (36)), which is discussed later in this section.

Therefore, the averaged strain tensors in both phases can be numerically solved on the basis of the standard backward Eulerian method. Similarly, in the other particle–matrix with the range of $d_2 \leqslant X_3 \leqslant t$ (zone III), the averaged strain fields are also solved by interchanging the matrix and particle phases.

For the transition zone II ($d_1 < X_3 < d_2$), the particle and matrix phases are not well defined because the two phases interpenetrate into one other as a connected network. Similarly to Reiter and Dvorak (1998), a phenomenological transition function is introduced to represent the continuous microstructural transition from zone I to III. Two sets of solutions are first calculated for zones I and III by extending the respective zone boundaries. Then, a cubic Hermite function is introduced to combine the contributions from both solutions as

$$\langle \boldsymbol{\varepsilon} \rangle^{A \text{ or } B}_{\text{zone-II}}(X_3) = f(X_3) \langle \boldsymbol{\varepsilon} \rangle^{A \text{ or } B}_{\text{zone-I}}(X_3) + [1 - f(X_3)] \langle \boldsymbol{\varepsilon} \rangle^{A \text{ or } B}_{\text{zone-III}}(X_3), \tag{30}$$

where the Hermite-type transition function (Yin et al., 2004) is given by

$$f(X_3) = \left[1 - 2 \frac{\phi(X_3) - \phi(d_1)}{\phi(d_1) - \phi(d_2)} \right] \left[\frac{\phi(X_3) - \phi(d_2)}{\phi(d_1) - \phi(d_2)} \right]^2. \tag{31}$$

The above treatment allows the averaged strain distributions for both phases to be continuous and differentiable in the gradation direction. However, because the microstructure of the transition zone is not truly characterized, this treatment only provides a phenomenological approximation for the averaged strain in the transition zone in lieu of a rigorous physics-based solution. For some composites, particles may be clustered and form a continuous network even at a relative low volume fraction (Agrawal et al., 2003). The transition zone in such FGMs may thus extend to a wide range. To predict the effective material properties in the transition zone with increased accuracy, a rigorous characterization of the microstructure is ultimately needed (Torquato, 2002).

Once the averaged strain distribution of each phase along the gradation direction is solved, the overall averaged strain at each layer can be further obtained from Eq. (25). From the relation between the averaged strain and the temperature change, the effective CTE distribution in the FGM gradation direction can be derived as

$$\bar{\boldsymbol{\alpha}}(X_3) = \frac{\langle \boldsymbol{\varepsilon} \rangle(X_3)}{T}. \tag{32}$$

Because thermal shear strains are not present, $\bar{\boldsymbol{\alpha}}(X_3)$ has only three non-zero components, among which, $\bar{\alpha}_{11} = \bar{\alpha}_{22}$ due to the symmetry in the $x_1 - x_2$ plane (see Fig. 1). However, $\bar{\alpha}_{33} \neq \bar{\alpha}_{11}$ because the averaged strains in the gradation direction is different from those in

other directions due to the particle interactions. Thus, even though both phases of the FGM are isotropic, the effective CTEs are no longer isotropic.

For an actual free-standing FGM under distributed temperature loading in the gradation direction, using the CTE distribution in Eq. (32), the thermal strain distribution can be given as follows:

$$\boldsymbol{\varepsilon}(X_3) = \bar{\boldsymbol{\alpha}}(X_3)T(X_3) \tag{33}$$

with $\varepsilon_{12} = \varepsilon_{23} = \varepsilon_{31} = 0$. However, from the strain compatibility conditions,

$$\varepsilon_{23,23} = \frac{1}{2}\left(\varepsilon_{22,33} + \varepsilon_{33,22}\right), \quad \varepsilon_{31,31} = \frac{1}{2}\left(\varepsilon_{33,11} + \varepsilon_{11,33}\right), \tag{34}$$

in which $\varepsilon_{23,23} = \varepsilon_{31,31} = \varepsilon_{33,22} = \varepsilon_{33,11} = 0$. If $\varepsilon_{11}(X_3)$ and $\varepsilon_{22}(X_3)$ are nonlinearly distributed in the X_3 direction, their second derivatives in Eq. (34) will not be zero, so the strain compatibility conditions are not met. Therefore, thermal stress must be induced to make the strain compatible. However, in some specific situations such as $\varepsilon_{11}(X_3)$ and $\varepsilon_{22}(X_3)$ being constant or linear functions of X_3, the strain compatibility conditions are still valid and the FGMs will deform uniformly or curl with a constant curvature, so that no thermal stress is induced. It is noted that the singular thermal stress in multilayer structures can be avoided in FGMs due to the continuous material property distribution along the gradation direction.

The proposed method aims at the thermomechanical behavior of FGMs. However, if the gradient of the microstructure is zero or if the particle volume fraction is constant in any direction, this model is still applicable to the uniform composites containing randomly dispersed particles. In this case, Eq. (23) is reduced to

$$\langle\boldsymbol{\varepsilon}\rangle^A = \alpha^A T\boldsymbol{\delta} + (\mathbf{I} - \mathbf{P}_0 \cdot \Delta\mathbf{C})^{-1} : \left(\langle\boldsymbol{\varepsilon}\rangle^B - \alpha^A T\boldsymbol{\delta} - \mathbf{P}_0 \cdot \mathbf{C}^B : \boldsymbol{\varepsilon}^{\mathrm{T}}\right)$$
$$+ \phi\Delta\mathbf{C}^{-1} \cdot \mathbf{D} : \left(\langle\boldsymbol{\varepsilon}\rangle^B - \alpha^A T\boldsymbol{\delta} - \Delta\mathbf{C}^{-1} \cdot \mathbf{C}^B : \boldsymbol{\varepsilon}^{\mathrm{T}}\right). \tag{35}$$

Substituting Eq. (35) into Eq. (24) provides the averaged strain in phase B as

$$\langle\boldsymbol{\varepsilon}\rangle^B = \alpha^B T\boldsymbol{\delta} + \phi\Big\{\phi\left[(\mathbf{I} - \mathbf{P}_0 \cdot \Delta\mathbf{C})^{-1} + \phi\Delta\mathbf{C}^{-1} \cdot \mathbf{D}\right] + (1-\phi)\left(\mathbf{C}^A\right)^{-1} \cdot \mathbf{C}^B\Big\}^{-1}$$
$$\times \Big\{(\mathbf{I} - \mathbf{P}_0 \cdot \Delta\mathbf{C})^{-1} \cdot \left[(\mathbf{I} + \mathbf{P}_0 \cdot \mathbf{C}^B)\right] + \phi\Delta\mathbf{C}^{-1} \cdot \mathbf{D} \cdot \Delta\mathbf{C}^{-1} \cdot \mathbf{C}^A\Big\} : \boldsymbol{\varepsilon}^{\mathrm{T}}. \tag{36}$$

Inserting Eq. (36) into Eq. (35) and using Eqs. (25) and (32), one can calculate the effective CTE. The term related to $\mathbf{D}$ in Eq. (35) represents the interactions from other particles. Disregarding this term, Eq. (36) is reduced to

$$\langle\boldsymbol{\varepsilon}\rangle^B = \alpha^B T\boldsymbol{\delta} + \phi\Big\{\phi\mathbf{I} + (1-\phi)(\mathbf{I} - \mathbf{P}_0 \cdot \Delta\mathbf{C}) \cdot \left(\mathbf{C}^A\right)^{-1} \cdot \mathbf{C}^B\Big\}^{-1} \cdot \left[(\mathbf{I} + \mathbf{P}_0 \cdot \mathbf{C}^B)\right] : \boldsymbol{\varepsilon}^{\mathrm{T}}. \tag{37}$$

Solving for the overall averaged strain, one can obtain the effective CTE from Eq. (32) as

$$\bar{\alpha}_{11} = \bar{\alpha}_{22} = \bar{\alpha}_{33} = \alpha^B + \phi\left(\alpha^A - \alpha^B\right)\frac{K^A\left(3K^B + 4\mu^B\right)}{4\mu^B\left[\phi K^A + (1-\phi)K^B\right] + 3K^A K^B}, \tag{38}$$

where K^A and K^B are the bulk moduli of phases A and B, respectively. This prediction is the same as the former Kerner model (1956). Because this prediction is directly based on the solution for one particle embedded in the infinite domain and the particle interactions

have been disregarded, the original Kerner model does not directly take into account the particle interactions.

3.2. Results and discussion

To demonstrate the capability of the proposed model, the modeling predictions are compared with the experimental data of Ishibashi et al. (2000). Mo/SiO$_2$ FGMs were fabricated with Mo particles filled in the continuous, glassy SiO$_2$ matrix; and the effective CTE distribution was measured along the gradation direction. The material properties of Mo and SiO$_2$ are: $E^{Mo} = 324$ GPa; $v^{Mo} = 0.31$; $\alpha^{Mo} = 5.1 \times 10^{-6}$ C^{-1}; $E^{SiO_2} = 80.4$ GPa; $v^{SiO_2} = 0.18$; and $\alpha^{SiO_2} = 0.54 \times 10^{-6}$ C^{-1} (Ishibashi et al., 2000). The volume fraction of Mo is approximated by the function,

$$\phi(X_3) = 0.2\left(e^{-28(X_3-0.085)^2} - 0.1X_3 + 0.1\right). \tag{39}$$

Thus, the maximum volume fraction of Mo is about 0.22 at $X_3 \approx 0.085$ and only one particle matrix zone exists in this FGM. The corresponding SEM micrographs can be found in Ishibashi et al. (2000). Fig. 2 shows the comparisons of the predicted CTE distribution along the gradation direction with the experimental data. Because the volume fraction function of Mo particles is not monotonic, the effective CTE does not monotonically vary in the gradation direction but increases to the peak point and then decreases. The proposed model provides a relatively good agreement with the experimental data. However, because the particles are not perfectly spherical with identical size, the proposed model somewhat underestimates the experimental results at large volume fractions (small values of X_3).

Neubrand et al. (2002) measured CTE distribution in an Al/Al$_2$O$_3$ FGM with a linear gradient of volume fraction of Al particles. The material properties of Al and Al$_2$O$_3$ (Neubrand et al., 2002, Moon et al., 2005) are: $E^{Al} = 69$ GPa; $v^{Al} = 0.33$; $\alpha^{Al} = 23.1 \times 10^{-6}$ C^{-1}; $E^{Al_2O_3} = 390$ GPa; $v^{Al_2O_3} = 0.2$; and $\alpha^{Al_2O_3} = 7.7 \times 10^{-6}$ C^{-1}. In Fig. 3, Neubrand et al. (2002) used the Reuss and Voigt estimates to establish bounds for their experimental data. The proposed model was found to fit reasonably well with their experimental results, which lie just above the lower bound described by the Reuss estimate.

The effective CTE of a two-phase FGM not only depends on the individual CTE of constituent phases, but also depends on the difference in mechanical properties between the particle and matrix phases. The thermoelastic properties of two phases of FGMs can vary by more than an order of magnitude. For instance, the Young's modulus of graphite is as low as 9.0 GPa, whereas the modulus of silicon carbide can reach 468.8 GPa (Kingery et al., 1976). In addition, the CTE of silica is as low as 0.5×10^{-6} C^{-1} (Wong and Bollampally, 1999), whereas the CTE of aluminum can reach 23.1×10^{-6} C^{-1} (Neubrand et al., 2002). Typically, the effective CTE of a two-phase FGM varies in the range between the CTEs of the two phases. The variation of the effective CTE in the gradation direction depends on the volume fraction distribution. For some applications of FGMs in thermal barrier coatings, there exists a favorable effective CTE distribution to minimize the thermal stress, which can be achieved by properly selecting the material constituents and volume fraction distribution. This problem is further discussed in Section 4.2.

Fig. 4 illustrates the effect of the phase material properties on the effective CTE for FGMs with a linear volume fraction distribution $\phi(X_3) = X_3/t$. For convenience, we

$E^A=324.0GPa,\ v^A=0.31,\ \alpha^A=5.1\times10^{-6},\ E^B=80.4GPa,\ v^B=0.18,\ \alpha^B=0.54\times10^{-6}$
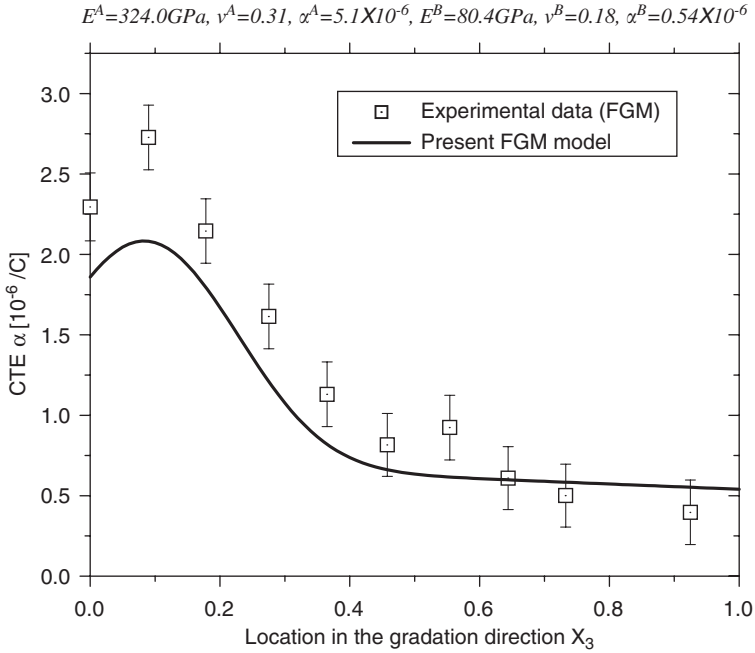
Fig. 2. Comparison of effective CTE distribution in a Mo/SiO$_2$ FGM using the experimental data of Ishibashi et al. (2000) and the present FGM model.

assume $v^A = v^B = 0.3$. The microstructural zone boundaries are selected with the corresponding volume fractions of 40% and 60%, respectively, which follows Bao and Cai's suggestion (1997). In Fig. 4(a), using $\alpha^A/\alpha^B = 10$, the normalized effective CTE increases with increasing Young's modulus in phase A. In each particle-matrix zone, when the particles are much stiffer than the matrix, further changing the particle Young's modulus will not produce a considerable effect on the effective CTE distribution. In the transition zone II, a continuous and differentiable jump of the effective CTE is observed. For $E^A \neq E^B$, a weak anisotropy of the effective CTE can be observed. In zone I, the effective CTE along the gradation direction is slightly lower than those in the other two directions, and vice versa in zone III. However, the difference is very small, so in the following only the CTE along the gradation direction is discussed. In Fig. 4(b), under the condition of $E^A/E^B = 10$, if the CTE for each phase is the same, i.e. $\alpha^A/\alpha^B = 1$, the effective CTE is constant since no thermal stress is induced. When the matrix is much stiffer than the particles, the effective CTE greatly depends on the matrix CTE.

When the volume fraction gradient of an FGM is reduced to zero or the particle volume fraction is constant in any direction, the proposed model is still applicable, e.g., for uniform composites containing randomly dispersed particles. Wong and Bollampally (1999) measured the CTE for spherical silica particle-filled epoxy composites. The material properties are given as: $E^{epoxy} = 2.25\,GPa$; $v^{epoxy} = 0.19$; $\alpha^{epoxy} = 88 \times 10^{-6}\,C^{-1}$; $E^{silica} = 73\,GPa$; $v^{silica} = 0.19$; and $\alpha^{silica} = 0.5 \times 10^{-6}\,C^{-1}$. Fig. 5 presents a comparison of the effective CTE as described by the experimental data, the proposed model, the Kerner model, and the Turner model (Kingery et al., 1976). The proposed model is found to be in

$E^A=69GPa, v^A=0.33, \alpha^A=23.1X10^{-6}, E^B=390GPa, v^B=0.21, \alpha^B=7.7X10^{-6}$
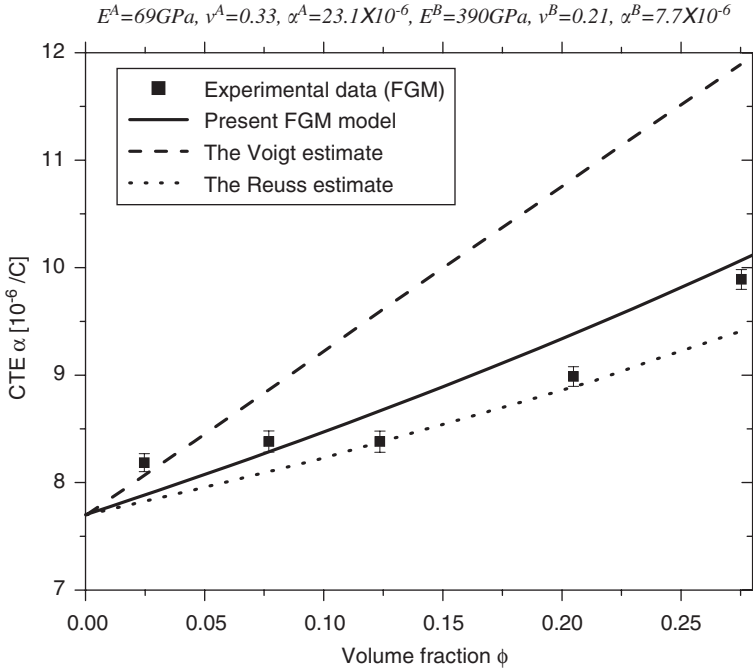
Fig. 3. Comparison of the effective CTE distribution in Al/Al$_2$O$_3$ FGM considering the experimental data (Neubrand et al., 2002), the proposed model, and also the Voigt and Reuss estimates.

excellent agreement with the experimental data, whereas the Turner model grossly underestimates the effective CTE. Because the epoxy matrix is much more compliant than the silica particles, it provides a relatively weak constraint on particle deformation. Therefore, the particle interactions produce a small effect, and the Kerner model yields a slightly higher prediction. However, these results still illustrate the benefits afforded by the current model, which explicitly accounts for particle interactions.

4. Thermal stress in graded TBCs

Graded TBCs have been widely used in propulsion and power-generation applications such as diesel engines, jet engines, and gas turbines (Schulz et al., 2003; Portinha et al., 2004). The reliability and functionality of coated components are strongly related to thermal stress in the graded materials (Karlsson et al., 2002; Balint and Hutchinson, 2005). When a hot FGM is deposited onto a uniform substrate and cooled down to room temperature, the device is subjected to a large temperature change, which causes a considerable thermal residual stress in the component. During the service life of a graded TBC, the surface is exposed to high temperatures, while the temperature in the substrate may be much lower. As a result, a strong heat flux will be induced within the coating. To simulate these two situations, in what follows, the thermal stress for graded TBCs bonded to a thick substrate are considered under two types of thermal loading: uniform temperature change and steady-state heat conduction.
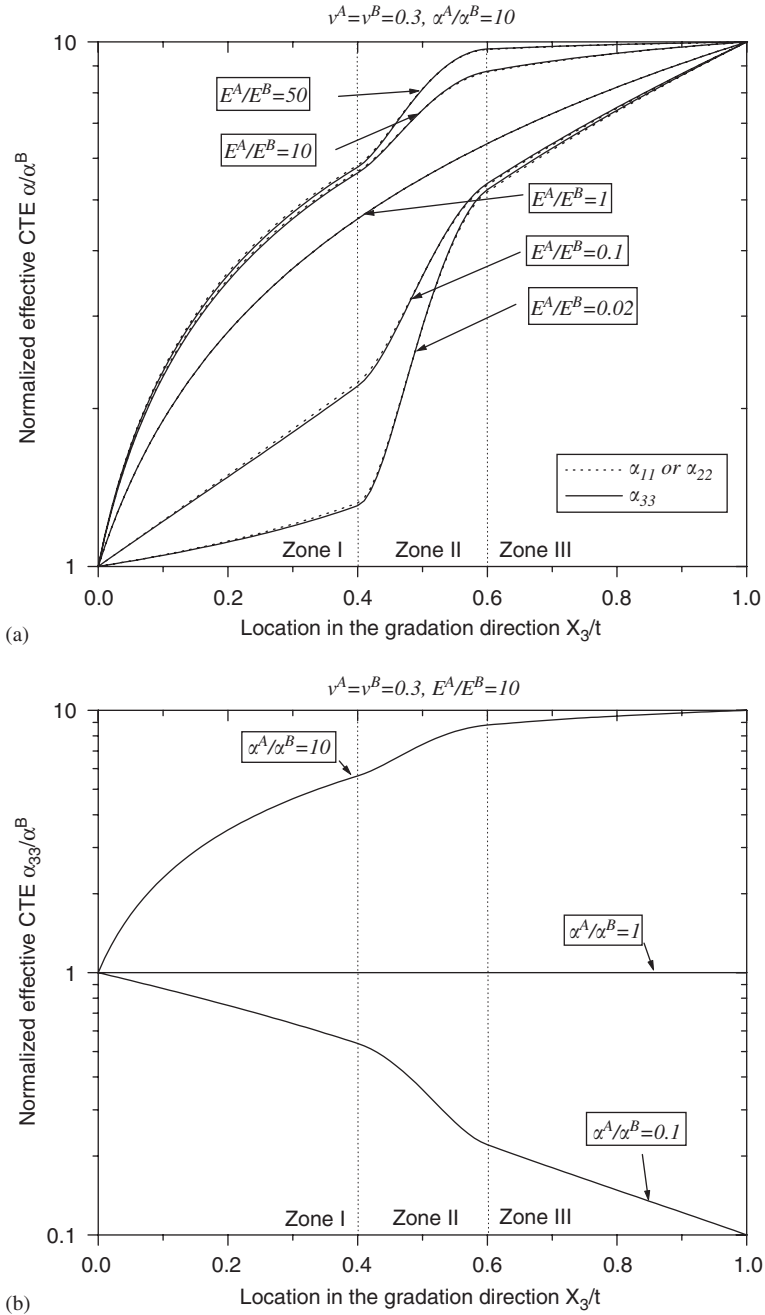
Fig. 4. Normalized effective CTE distribution in FGMs considering (a) Young's modulus contrast ratio and (b) CTE contrast ratio of two phases.

$E^A=73GPa, v^A=0.19, \alpha^A=0.5X10^{-6}, E^B=2.25GPa, v^B=0.19, \alpha^B=88X10^{-6}$
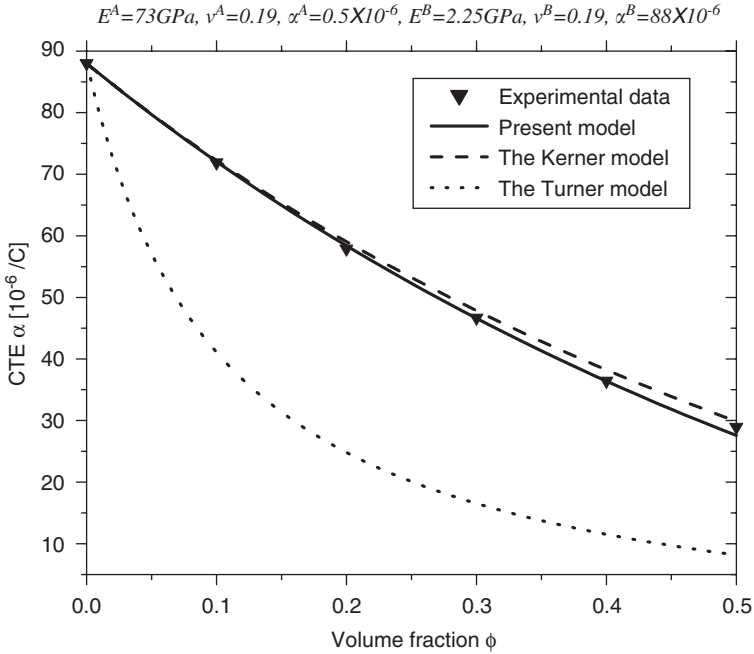
Fig. 5. Comparison of effective CTE of silica-filled epoxy composites considering the experimental data of Wong and Bollampally (1999), the proposed model, the Kerner model, and the Turner model (Kingery et al., 1976).

Consider a graded ceramic/metal TBC bonded to a thick metal substrate as illustrated in Fig. 6. The temperature changes on the surface of the TBC and at the interface between the TBC and the substrate are denoted as T^1 and T^2, respectively. It is assumed that the substrate is stiffer than the coating material and the thickness of TBC is much smaller than other dimensions (Teixeira, 2001; Rangaraj and Kokini, 2003). Thus, the deformation of the TBC in the X_1-X_2 plane is strongly constrained by the substrate, whereas the deformation in the X_3 direction is free. Since the thermal conductivity of the metal substrate is typically much higher than that of the coating, the temperature variation in the substrate should be small. Consequently, the thermal strain of the substrate is, for simplicity, assumed to be uniform. Although the TBC may provide a shear loading through the interface, especially at the ends of the coating, it will not affect the shape of the substrate because the coating is thin and compliant. Thus, the interface remains in plane. Consequently, it is approximated that the averaged strain components of the TBC in the X_1-X_2 plane are consistent with the deformation of the metal substrate, namely,

$$\langle \varepsilon_{11} \rangle (X_3) = \langle \varepsilon_{22} \rangle (X_3) = \varepsilon^s, \tag{40}$$

where ε^s denotes the strain of the substrate, typically determined by the CTEs and the boundary condition of the substrate. Due to the free surface of the TBC, it is written

$$\langle \sigma_{33} \rangle (X_3) = 0. \tag{41}$$

Thus, in the entire graded TBC, the strains $\langle \varepsilon_{11} \rangle$ and $\langle \varepsilon_{22} \rangle$ and stress $\langle \sigma_{33} \rangle$ are uniform. On the upper or lower boundary of the graded TBC, the material is either phase A or B, so,
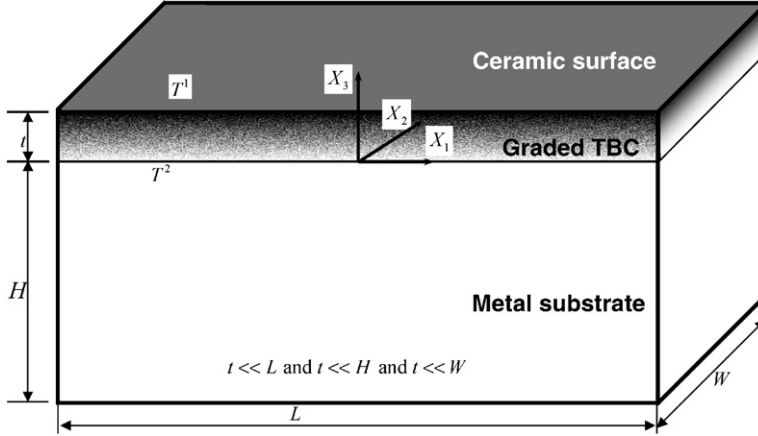
Fig. 6. Schematic illustration of a thin graded ceramic/metal TBC deposited onto a thick metal substrate and subjected to a thermal loading.

combining Eqs. (40) and (41), the averaged strain on the corresponding boundary can be solved. For instance, on the lower boundary, there exists

$$\langle \varepsilon_{11} \rangle^B(0) = \langle \varepsilon_{22} \rangle^B(0) = \varepsilon^s; \quad \langle \varepsilon_{33} \rangle^B(0) = \frac{1 + v^B}{1 - v^B} \alpha^B T - \frac{2v^B \varepsilon^s}{1 - v^B}. \tag{42}$$

Using Eqs. (40)–(42) along with the governing equations of Eqs. (23)–(27), the averaged strain distribution in each phase of the grade TBC can be derived. The overall thermal stress distribution in the FGM can then be obtained.

4.1. Graded TBCs under a uniform temperature change

First, consider the graded TBC under a uniform temperature change in the gradation direction of the FGM, i.e., $T^1 = T^2 = T$. In the following numerical simulations, the FGM TBC is made of NiCrAlY metal and $ZrO_2Y_2O_3$ ceramic, which are commonly used in duplex TBC systems (Teixeira, 2001) with a linear volume fraction distribution. The material constants are: $E^{NiCrAlY} = 170\,GPa$; $v^{NiCrAlY} = 0.25$; $\alpha^{NiCrAlY} = 12.5 \times 10^{-6}\,K^{-1}$; $E^{ZrO_2Y_2O_3} = 80\,GPa$; $v^{ZrO_2Y_2O_3} = 0.23$; and $\alpha^{ZrO_2Y_2O_3} = 8.6 \times 10^{-6}\,K^{-1}$ (Teixeira, 2001). The coating is deposited onto a stiffer substrate, which deforms with the temperature according to

$$\varepsilon^s = \alpha^{sub} T \tag{43}$$

with α^{sub} being the CTE of the substrate. It is noted that, although in the above equation it is assumed that the substrate strain ε^s is governed by the temperature change in the substrate, in general applications of TBCs, the variation of ε^s along the interface may also be related to the boundary conditions of the substrate, the thermomechanical property of the coating, and the geometry of the coating and the substrate. For simplicity of modeling, it is assumed that the mechanical properties of each phase of the FGMs are independent of temperature, and the deformation of the materials is always in the linear elastic range.

In Fig. 7, the thermal stress distributions are illustrated for the graded TBC deposited on four types of substrates and subjected to a temperature change of $T = -400K$. The substrates dictate uniform strains, namely: $\varepsilon^s = -0.002 \; -0.005$ and -0.01, which correspond to their CTEs, which are: 5; 12.5, and 25 ($\times 10^{-6} \, K^{-1}$), respectively. Since the metal phase of the TBC is stiffer than the ceramic phase, the thermal stress in the metal-rich end is more sensitive to the change of ε^s than that of the ceramic-rich end. Unlike the discontinuous thermal stress in multi-layer structures (Teixeira, 2001), the thermal stress of the graded TBC continuously varies in the gradation direction. When the CTE of the substrate is higher than that of each layer of the coating, the thermal stress in the coating is compressive; and vice versa. To reduce the thermal stress, the CTE of the stiffer phase should be selected close to the CTE of the substrate. In the actual material system, the tensile strength of $ZrO_2Y_2O_3$ ceramic may vary across a wide range, e.g. from 15 MPa to 800 MPa (Choi et al., 2004, Kondoh et al., 2004), which depends on the testing temperature and the chemical composition of the stabilizer. The stresses are presented here in the context that they are not higher than the material strength for each material phase.

When the CTE of the substrate matches that of NiCrAlY, the strain of the substrate will be $\varepsilon^s = -0.005$. Fig. 8 compares the averaged thermal stresses of each phase with the overall stress distributed in the gradation direction of the TBC. Although the overall thermal stress varies smoothly, the stress in each phase may not vary monotonically in the gradation direction due to the interchange of the particle and matrix phases through the transition zone. In Fig. 8(a), because phase A is much more compliant than phase B and the substrate has the same CTE as phase B, the compressive thermal stress of phase A

$E^A=80.0GPa, \; v^A=0.23, \; \alpha^A=8.6 X10^{-6}, \; E^B=170GPa, \; v^B=0.25,$
$\alpha^B=12.5 X10^{-6}, \; T=-400$
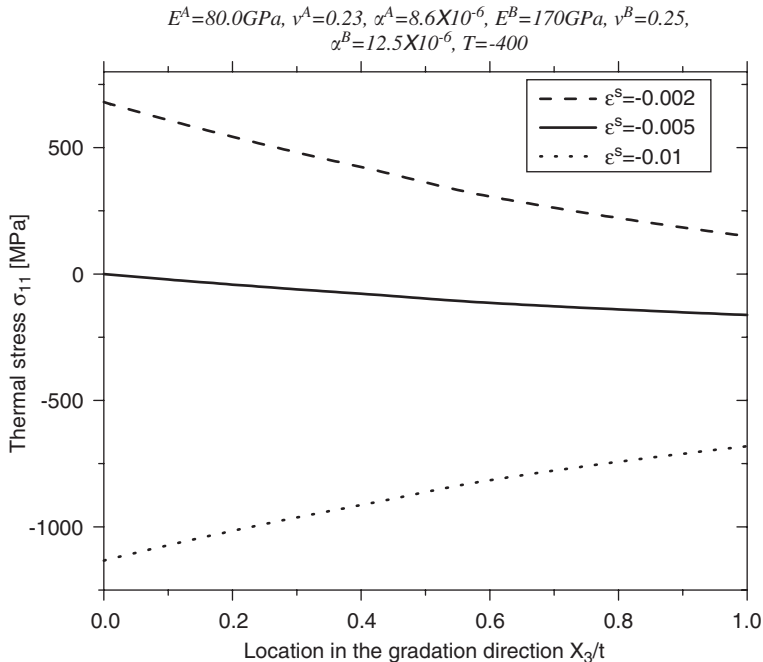
Fig. 7. Thermal stress distributions in the graded TBC subjected to a uniform temperature change and the constraint strains from different types of substrates.
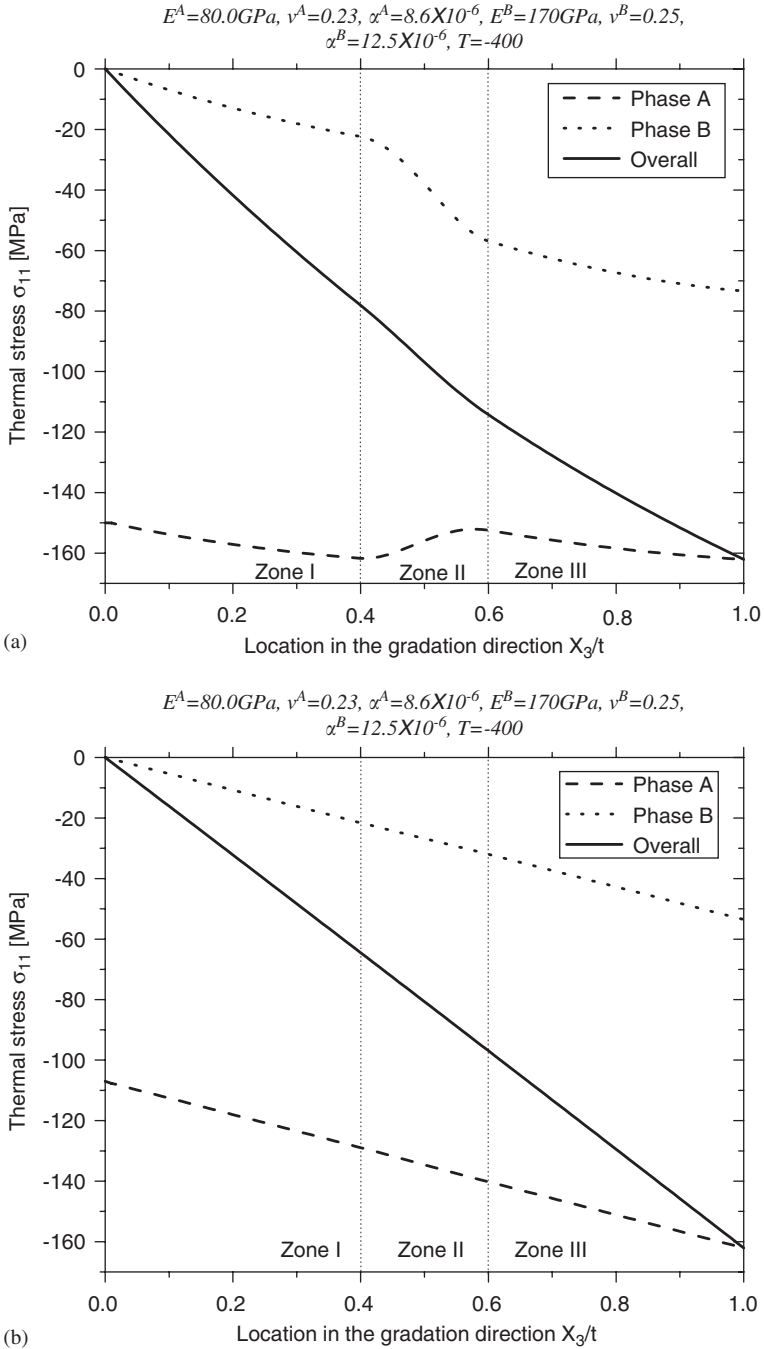
Fig. 8. Thermal stress distribution of each phase and FGM layer in the TBC subjected to a uniform temperature change and a substrate strain $\varepsilon^s = -0.005$ for different Young's modulus contrast ratios: (a) $E^B/E^A = 2.125$; (b) $E^B/E^A = 1$.

increases along with its volume fraction in zones I and III, whereas it decreases in zone II due to the exchange of the particle and matrix phases. However, when the elastic mismatch between two phases is smaller, the variation of thermal stress for each phase will be smoother. By setting $E^B/E^A = 1$ in Fig. 8(b), the three curves are all linear, as expected. To reduce the variation of thermal stress for each phase in the gradation direction, differences in the elastic moduli between phases of the graded TBC should be minimized to the extent possible.

4.2. Graded TBCs under a steady-state heat flux

During service, the surface of the coating typically is exposed to a higher temperature, whereas the substrate material stays at a relatively low temperature. An approximately steady-state temperature field exists in the coating. Since the effective thermal conductivity of the graded TBC varies spatially in the coating, the temperature field will not linearly change in the gradation direction. In our recent work (Yin et al., 2005), given the thermal properties of each phase and the volume fraction distribution of an FGM, the effective thermal conductivity distribution is successfully predicted. Then, given the temperature boundary conditions in the surface and the bottom of the coating, the heat flux in the gradation direction can be solved, and the temperature profile can be calculated. Once the temperature distribution is obtained, similarly to the previous subsection, the overall thermal stress distribution and thermal stress in each phase can be obtained.

In the following simulations, the same graded TBC is used, which contains the NiCrAlY metal and the $ZrO_2Y_2O_3$ ceramic with a linear volume fraction distribution. Initially, the TBC is assumed to be unrestrained and free of any thermal residual stresses in either phase. The temperature changes on the surface and bottom are $T^1 = 400\,K$ and $T^2 = 275\,K$, respectively. The thermal conductivities of NiCrAlY and $ZrO_2Y_2O_3$ are used as 12.5 and 1.8 W/K, respectively (Teixeira et al., 1999). Then the effective conductivity distribution and the temperature profile are obtained as shown in Fig. 9 (Yin et al., 2005). Because the effective conductivity decreases in the gradation direction, the temperature distribution curve is downward convex. Thus, in the metal-rich range, the temperature changes slowly, whereas in the ceramic-rich range, the temperature increases rapidly.

If the substrate is assumed with the same CTE as NiCrAlY, the overall thermal stress at the bottom of the coating is always zero. Fig. 10 shows the thermal stress distributions of both phases and overall thermal stress in the gradation direction due to a steady-state thermal loading. The overall thermal stress is always close to zero, whereas the tensile stress in phase *A* and the compressive stress in phase *B* may be in excess of 100 MPa. Since the effective CTE of the TBC decreases while the temperature increases along the gradation direction, the overall thermal strain in the TBC is very close to the one in the substrate. Therefore, the substrate provides a relatively small constraint and the overall thermal stress in the TBC is small. However, at any material point, since there is a mismatch of CTEs between phases, thermal stresses will be induced in each phase and will be proportional to the temperature change.

Fig. 11 compares the thermal stress for the TBC under the steady-state thermal loading to those of the TBC under uniform temperature changes of $T = 275$ and $400\,K$, respectively. Although the temperature field of the TBC is in the range of 275–400 K for the steady-state thermal loading, the thermal stress for the varying temperature field is much lower than the stress for each uniform temperature change, either 275 or 400 K. If, at
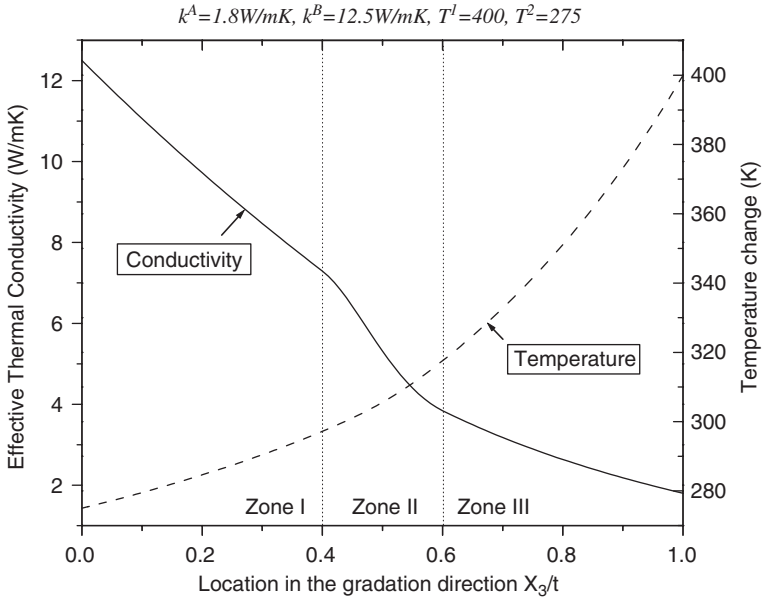
Fig. 9. Thermal conductivity and temperature distributions in the graded TBC subjected to a steady-state thermal loading.
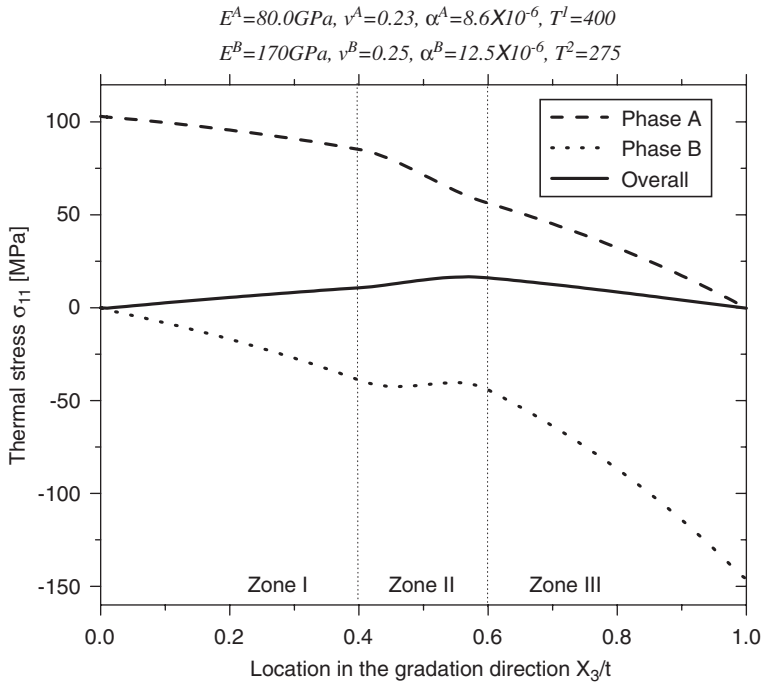
Fig. 10. Thermal stress distributions of each phase and FGM layer in the TBC subjected to a steady-state thermal loading.

$E^A=80.0GPa$, $v^A=0.23$, $\alpha^A=8.6 \times 10^{-6}$, $E^B=170GPa$, $v^B=0.25$,
$\alpha^B=12.5 \times 10^{-6}$
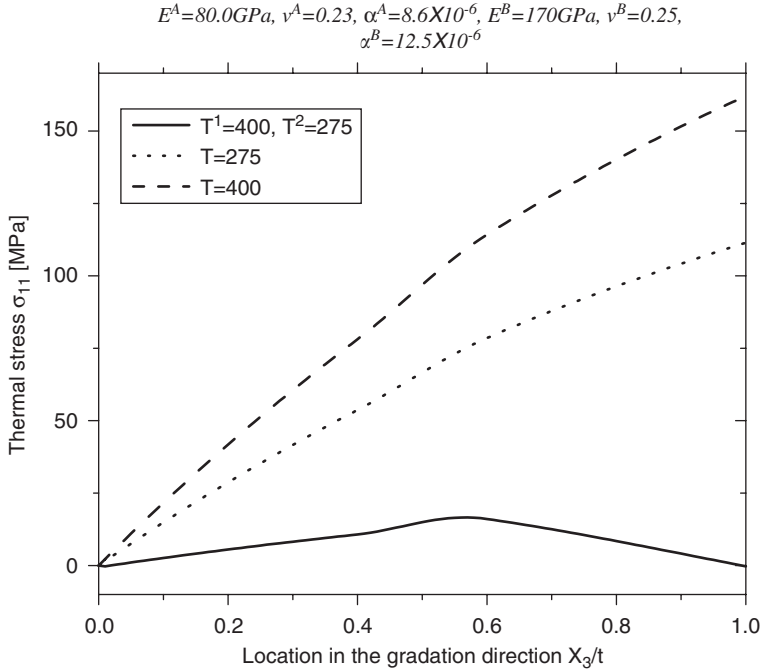
Fig. 11. Comparisons of the thermal stress in a graded TBC subjected to three cases of thermal loadings: a steady-state thermal loading (solid curve) and two uniform temperature changes (dashed and dotted curves).

any material point, there exists

$$\bar{\alpha}(X_3)T(X_3) = \varepsilon^s, \tag{44}$$

where $\bar{\alpha}(X_3)$ refers to the components of effective CTE in the corresponding X_1–X_2 plane, then, the overall thermal stress can be reduced to zero. For a gradually varying temperature field in the coating, one can achieve the goal of eliminating thermal stress by properly selecting the materials to optimize the microstructure. However, for given temperature boundary conditions, because both the temperature field and the effective CTE in the TBC are related to the microstructure, an iterative optimization method must be employed. An extension of this work to the design of TBCs for specific applications is underway.

5. Conclusions

A micromechanics-based thermoelastic model is developed for two-phase functionally graded particulate materials. The Eshelby's equivalent inclusion method is employed to derive the local elastic field under thermomechanicial loading and to define the pair-wise thermoelastic interaction. For a material point, a graded RVE is constructed to represent the microstructure at the microscopic scale. By integrating all the pair-wise interactions from other particles in the RVE, a set of governing equations is obtained for the thermoelastic behavior of FGMs. Using the governing equations and considering the stress-free condition over the RVE, the averaged thermal strain distribution in the

gradation direction is solved and then the effective CTE is obtained, which is shown to be weakly anisotropic and continuously varying in the gradation direction. When the material gradient is reduced to zero, the proposed model predicts the effective CTE for uniform composites. If the particle interactions are disregarded, the proposed model recovers the well-known Kerner model. These features demonstrates the consistency of the proposed approach. Furthermore, the proposed model is employed to calculate the thermal stress distributions for graded TBCs deposited onto thick, stiff substrates. Two types of thermal loading are considered: uniform temperature change and steady-state heat conduction in the gradation direction. The effect of the stiffness and CTE of both phases on the thermal stress distribution is discussed. The micromechanics framework presented in this work is general and has recently been extended to damage of particulate FGMs (Paulino et al, 2006).

Acknowledgments

Appendix A. Thermomechanical solution for two particles in an infinite domain

For two identical spherical particles Ω_0 and Ω_1 embedded in the infinite domain under a uniform temperature change T and a far field elastic strain ε_{ij}^0, the local elastic field can be solved by the equivalent inclusion method (Moschovidis and Mura, 1975). Due to the particle interactions, the elastic equivalent eigenstrain of the particles is no longer uniform. The elastic equivalent eigenstrain of particle Ω_0 centered at the origin can be extended in terms of polynomial form of local coordinates as

$$\varepsilon_{ij}^*(\mathbf{x}) = B_{ij}^0 + B_{ijk}^1 x_k + \cdots \quad \mathbf{x} \in \Omega_0. \tag{45}$$

Because the symmetry of the geometry, the eigenstrain in the other particle Ω_1 centered at $\mathbf{x}^1$ is written as

$$\varepsilon_{ij}^*(\mathbf{x}) = B_{ij}^0 + B_{ijk}^1 \left(x_k^1 - x_k \right) + \cdots + \mathbf{x} \in \Omega_1. \tag{46}$$

Then, the perturbed strain due to material mismatch is written as

$$\varepsilon'(\mathbf{x}) = - \int_{\Omega_0} \mathbf{\Gamma}(\mathbf{x} - \mathbf{x}') \cdot \mathbf{C}^B : \left[\varepsilon^*(\mathbf{x}') + \varepsilon^{\mathrm{T}} \right] d\mathbf{x}' - \int_{\Omega_1} \mathbf{\Gamma}(\mathbf{x} - \mathbf{x}') \cdot \mathbf{C}^B : \left[\varepsilon^*(\mathbf{x}') + \varepsilon^{\mathrm{T}} \right] d\mathbf{x}'. \tag{47}$$

Substituting Eq. (47) into Eq. (1) provides the strain field in particle Ω_0 as

$$\begin{aligned} \varepsilon_{ij}(\mathbf{x}) = \varepsilon_{ij}^0 &- P_{ijkl}^0 C_{klmn}^B \left(B_{mn}^0 + \varepsilon_{mn}^{\mathrm{T}} \right) - Q_{ijklp}^0(\mathbf{x}) C_{klmn}^B B_{mnp}^1 \\ &- P_{ijkl}\left(\mathbf{x} - \mathbf{x}^1 \right) C_{klmn}^B \left(B_{mn}^0 + \varepsilon_{mn}^{\mathrm{T}} \right) + Q_{ijklp}\left(\mathbf{x} - \mathbf{x}^1 \right) C_{klmn}^B B_{mnp}^1, \end{aligned} \tag{48}$$

where

$$
Q_{ijklp}^0(\mathbf{x}) = \frac{1}{140\mu^B(1-v^B)}
\begin{bmatrix}
2\delta_{jp}\delta_{kl}x_i + (7v^B - 5)(\delta_{kp}\delta_{jl} + \delta_{kj}\delta_{lp})x_i \\
+2\delta_{ip}\delta_{kl}x_j + (7v^B - 5)(\delta_{kp}\delta_{il} + \delta_{ki}\delta_{lp})x_j \\
+2\delta_{ij}\delta_{pl}x_k + (7v^B - 5)(\delta_{ip}\delta_{jl} + \delta_{il}\delta_{jp})x_k \\
+2\delta_{ij}\delta_{pk}x_l + (7v^B - 5)(\delta_{ip}\delta_{jk} + \delta_{ik}\delta_{jp})x_l \\
+2\delta_{ij}\delta_{kl}x_p + (14v^B - 12)(\delta_{ik}\delta_{jl} + \delta_{il}\delta_{jk})x_p
\end{bmatrix},
\tag{49}
$$

and

$$
Q_{ijklp}(\mathbf{x} - \mathbf{x}^1) = \frac{a\rho^4}{140\mu^B(1-v^B)}
$$

$$
\times
\begin{bmatrix}
(7 - 5\rho^2)\delta_{jp}\delta_{kl}n_i + (7v^B - 5\rho^2)(\delta_{kp}\delta_{jl} + \delta_{kj}\delta_{lp})n_i \\
+(7 - 5\rho^2)\delta_{ip}\delta_{kl}n_j + (7v^B - 5\rho^2)(\delta_{kp}\delta_{il} + \delta_{ki}\delta_{lp})n_j \\
+(7 - 5\rho^2)\delta_{ij}\delta_{pl}n_k + (7v^B - 5\rho^2)(\delta_{ip}\delta_{jl} + \delta_{il}\delta_{jp})n_k \\
+(7 - 5\rho^2)\delta_{ij}\delta_{pk}n_l + (7v^B - 5\rho^2)(\delta_{ip}\delta_{jk} + \delta_{ik}\delta_{jp})n_l \\
+(7 - 5\rho^2)\delta_{ij}\delta_{kl}n_p + (14v^B - 7 - 5\rho^2)(\delta_{ik}\delta_{jl} + \delta_{il}\delta_{jk})n_p \\
-35(1 - \rho^2)(\delta_{ij}n_kn_l + \delta_{kl}n_in_j)n_p \\
-35(v^B - \rho^2)(\delta_{ik}n_jn_ln_p + \delta_{il}n_jn_kn_p + \delta_{jk}n_in_ln_p + \delta_{jl}n_in_kn_p) \\
+35(1 - \rho^2)(\delta_{pk}n_jn_ln_i + \delta_{pl}n_jn_kn_i + \delta_{pi}n_jn_kn_l + \delta_{pj}n_in_kn_l) \\
+35(7 - 9\rho^2)n_in_jn_kn_ln_p
\end{bmatrix}.
\tag{50}
$$

The strain in particle Ω_0 must satisfy the stress equivalent formulation in Eq. (6). Because the particle strain field is neither uniformly nor linearly distributed, Eq. (6) cannot be strictly satisfied by introducing a linear eigenstrain as Eq. (45). However, the strain field of Eq. (48) can be extended in terms of polynomial form of local coordinates. Using Eq. (6), it is obtained

$$
\Delta C_{ijkl}^{-1} C_{klmn}^B B_{mn}^0 = -\varepsilon_{ij}^0 + \alpha^A T \delta_{ij} + \left(P_{ijkl}^0 + P_{ijkl}(-\mathbf{x}) \right) C_{klmn}^B \left(B_{mn}^0 + \varepsilon_{mn}^T \right)
$$
$$
- Q_{ijklp}(-\mathbf{x}^1) C_{klmn}^B B_{mnp}^1,
$$
$$
\Delta C_{ijkl}^{-1} C_{klmn}^B B_{mnp}^1 = P_{ijkl,p}(-\mathbf{x}^1) C_{klmn}^0 \left(B_{mn}^0 + \varepsilon_{mn}^T \right) + Q_{ijklq,p}^0(\mathbf{0}) C_{klmn}^B B_{mnq}^1
$$
$$
- Q_{ijklq,p}(-\mathbf{x}^1) C_{klmn}^B B_{mnq}^1.
\tag{51}
$$

Solving the above equations for $\mathbf{B}^0$ and $\mathbf{B}^1$ provides

$$
\mathbf{B}^0 = (\mathbf{C}^B)^{-1} \cdot \left[\mathbf{P}^0 + \mathbf{P}(-\mathbf{x}^1) - \Delta\mathbf{C}^{-1} \right]^{-1} : \left\{ \boldsymbol{\varepsilon}^0 - \alpha^A T \boldsymbol{\delta} \right.
$$
$$
\left. - \left[\mathbf{P}^0 + \mathbf{P}(-\mathbf{x}^1) \right] \cdot \mathbf{C}^B : \boldsymbol{\varepsilon}^T \right\} + O(\rho^8),
$$
$$
\mathbf{B}^1 = O(\rho^4).
\tag{52}
$$

It is noted that, from Eq. (11), there exists $\mathbf{P}(\mathbf{x}^1) = \mathbf{P}(-\mathbf{x}^1)$. Substituting Eq. (52) into Eq. (48) yields the local strain field. Considering an average over particle Ω_0, one can find

that the third term in the right-hand side of Eq. (48) vanishes, the fifth term is of order $O(\rho^8)$, and then the averaged strain of particles is written as

$$\bar{\boldsymbol{\varepsilon}}_{\Omega} = \alpha^A T \boldsymbol{\delta} + \left\{ \mathbf{I} - \left[\mathbf{P}^0 + \mathbf{P}(\mathbf{x}^1) \right] \cdot \Delta\mathbf{C} \right\}^{-1} : \left\{ \boldsymbol{\varepsilon}^0 - \alpha^A T \boldsymbol{\delta} - \left[\mathbf{P}^0 + \mathbf{P}(\mathbf{x}^1) \right] \cdot \mathbf{C}^B : \boldsymbol{\varepsilon}^T \right\} + O(\rho^8). \tag{53}$$

Appendix B. Explicit form and integrals of the pairwise interaction tensor

Based on the method of Ju and Chen (1994), the pair-wise interaction tensor in Eq. (13) can be explicitly derived as

$$\begin{aligned} L_{ijkl}\left(\mathbf{0}, \mathbf{x}^1\right) &= c_1 \delta_{ij}\delta_{kl} + c_2\left(\delta_{ik}\delta_{jl} + \delta_{il}\delta_{jk}\right) + c_3\left(\delta_{ij}n_k n_l + \delta_{kl}n_i n_j\right) \\ &\quad + c_4\left(\delta_{ik}n_j n_l + \delta_{il}n_j n_k + \delta_{jk}n_i n_l + \delta_{jl}n_i n_k\right) + c_5 n_i n_j n_k n_l, \end{aligned} \tag{54}$$

where the coefficients c_i $(i = 1, 2, \ldots, 5)$ are defined as

$$\begin{aligned} c_1 &= \frac{-d_1(2d_2 + 4d_4 + d_5) + d_3^2}{4d_2\left[d_1(3d_2 + 4d_4 + d_5) + d_2(2d_2 + 2d_3 + 4d_4 + d_5) - d_3^2\right]} + \frac{\alpha}{2\beta(3\alpha + 2\beta)}, \\ c_2 &= \frac{1}{4d_2} - \frac{1}{4\beta}, \\ c_3 &= \frac{-d_1(4d_4 + d_5) - 2d_2 d_3 - d_3^2}{4d_2\left[d_1(3d_2 + 4d_4 + d_5) + d_2(2d_2 + 2d_3 + 4d_4 + d_5) - d_3^2\right]}, \\ c_4 &= -\frac{d_4}{4d_2(d_2 + d_4)}, \\ c_5 &= \frac{d_2\left(8d_3 d_4 + 3d_3^2 - 3d_1 d_5 - 2d_2 d_5 + 2d_4 d_5 + 8d_4^2\right) + d_1 d_4(4d_4 + d_5) - d_3^2 d_4}{4d_2(d_2 + d_4)\left[d_1(3d_2 + 4d_4 + d_5) + d_2(2d_2 + 2d_3 + 4d_4 + d_5) - d_3^2\right]}, \end{aligned} \tag{55}$$

in which

$$\begin{aligned} d_1 &= \alpha - \frac{\rho^3}{60\mu^B(1 - v^B)}\left(5 - 3\rho^2\right), \\ d_2 &= \beta + \frac{\rho^3}{60\mu^B(1 - v^B)}\left(5 - 10v^B + 3\rho^2\right), \\ d_3 &= \frac{\rho^3}{4\mu^B(1 - v^B)}\left(1 - \rho^2\right), \\ d_4 &= \frac{\rho^3}{4\mu^B(1 - v^B)}\left(v^B - \rho^2\right), \\ d_5 &= -\frac{\rho^3}{4\mu^B(1 - v^B)}\left(5 - 7\rho^2\right) \end{aligned} \tag{56}$$

and

$$\alpha = -\frac{\lambda^A - \lambda^B}{2(\mu^A - \mu^B)\left[3(\lambda^A - \lambda^B) + 2(\mu^A - \mu^B)\right]} - \frac{1}{30\mu^B(1 - v^B)},$$

$$\beta = \frac{1}{4(\mu^A - \mu^B)} + \frac{4 - 5v^B}{30\mu^B(1 - v^B)}. \tag{57}$$

Here, λ is the first Lamé constant, and superscripts A and B denote the particle phase A and the matrix phase B, respectively.

To integrate the pair-wise interaction of all other particles in the RVE on the central particle, Eq. (20) is obtained, in which the tensors $\mathbf{D}$ and $\mathbf{F}$ are written as:

$$\mathbf{D}(0) = \int_D \frac{3g(x)}{4\pi a^3} \mathbf{L}(\mathbf{0}, \mathbf{x}) \, \mathrm{d}\mathbf{x},$$

$$\mathbf{F}(0) = \int_D e^{-x/\delta} \frac{3g(x)}{4\pi a^3} \mathbf{L}(\mathbf{0}, \mathbf{x}) x_3^2 \, \mathrm{d}\mathbf{x}. \tag{58}$$

Here, the volume element can be further written as $\mathrm{d}\mathbf{x} = x^2 \mathrm{d}\omega \mathrm{d}x$, where $\mathrm{d}\omega$ is the surface element on the unit sphere Σ centered at the origin of the coordinates. Because $g(x) = 0$ for $x < 2a$, the above equation can be rewritten as

$$\mathbf{D}(0) = \int_{2a}^{\infty} \frac{3g(x)}{4\pi a \rho^2} \int_{\Sigma} \mathbf{L}(\mathbf{0}, \mathbf{x}) \, \mathrm{d}\omega \, \mathrm{d}x,$$

$$\mathbf{F}(0) = \int_{2a}^{\infty} \mathrm{e}^{-x/\delta} \frac{3g(x)a}{4\pi \rho^4} \int_{\Sigma} \mathbf{L}(\mathbf{0}, \mathbf{x}) n_3^2 \, \mathrm{d}\omega \, \mathrm{d}x. \tag{59}$$

Using Eq. (54), it is derived

$$\int_{\Sigma} L_{ijkl}(\mathbf{0}, \mathbf{x}) \, \mathrm{d}\omega = \frac{4\pi}{15}(15c_1 + 10c_3 + c_5)\delta_{ij}\delta_{kl} + \frac{4\pi}{15}(15c_2 + 10c_4 + c_5)\left(\delta_{ik}\delta_{jl} + \delta_{il}\delta_{jk}\right) \tag{60}$$

and

$$\int_{\Sigma} L_{ijkl}(0, \mathbf{x}) n_3^2 \, \mathrm{d}\omega = \frac{4\pi}{105}[35c_1 + 14c_3 + c_5 + 2(7c_3 + c_5)(\delta_{I3} + \delta_{K3})]\delta_{ij}\delta_{kl}$$

$$+ \frac{4\pi}{105}[35c_2 + 14c_4 + c_5 + 2(7c_4 + c_5)(\delta_{I3} + \delta_{J3})]\left(\delta_{ik}\delta_{jl} + \delta_{il}\delta_{jk}\right). \tag{61}$$

Substituting Eqs. (60) and (61) into (59) gives Eqs. (21) and (22).

References

Aboudi, J., Pindera, M.-J., Arnold, S.M., 1999. Higher-order theory for functionally graded materials. Compos. B 30 (8), 777–832.

Agrawal, P., Gonlon, K., Bowman, K.J., Sun, C.T., Cichocki, F.R., Trumble, K.P., 2003. Thermal residual stresses in co-continuous composites. Acta Mater. 51 (4), 1143–1156.

Balint, D.S., Hutchinson, J.W., 2005. An analytical model of rumpling in thermal barrier coatings. J. Mech. Phy. Solids 53 (4), 949–973.

Bao, G., Cai, H., 1997. Delamination cracking in functionally graded coating/metal substrate systems. Acta Mater. 45 (3), 1055–1066.

Budiansky, B., 1965. On the elastic moduli of some heterogeneous materials. J. Mech. Phys. Solids 13 (4), 223–227.

Buryachenko, V.A., Rammerstofer, F.G., 2001. Local effective thermoelastic properties of graded random structure materix composites. Arch. App. Mech. 71 (4-5), 249–272.

Choi, S.R., Zhu, D., Miller, R.A., 2004. Mechanical properties/database of plasma-sprayed ZrO_2-8wt% Y_2O_3 thermal barrier coatings. Int. J.App. Ceram. Technol. 1 (4), 330–342.

Cowin, S.C., Mehrabadi, M.M., 1995. Anisotropic symmetries of linear elasticity. App. Mech. Rev. 48 (5), 247–285.

Dao, M., Gu, P., Maewal, A., Asaro, R.J., 1997. A micromechanical study of residual stresses in functionally graded materials. Acta. Mater. 45 (8), 3265–3276.

Drugan, W.J., 2000. Micromechanics-based variational estimates for a higher-order nonlocal constitutive equation and optimal choice of effective moduli for elastic composites. J. Mech. Phys. Solids 48 (6–7), 1359–1387.

Drugan, W.J., 2003. Two exact micromechanics-based nonlocal constitutive equations for random linear elastic composite materials. J. Mech. Phys. Solids 51 (9), 1745–1772.

Drugan, W.J., Willis, J.R., 1996. A micromechanics-based nonlocal constitutive equation and estimates of representative volume element size for elastic composites. J. Mech. Phys. Solids 44 (4), 497–524.

Eischen, J.W., 1987. Fracture of nonhomogeneous materials. Int. J. Fract. 34 (1), 3–22.

Eshelby, J.D., 1957. The determination of the elastic field of an ellipsoidal inclusion, and related problems. Proc. Roy. Soc. A 241 (1226), 376–396.

Eshelby, J.D., 1959. The elastic field outside an ellipsoidal inclusion. Proc. Roy. Soc. A 252 (1271), 561–569.

Hill, R., 1965. A self-consistent mechanics of composite materials. J. Mech. Phys. Solids 13 (4), 213–222.

Ishibashi, H., Tobimatsu, H., Matsumoto, T., Hayashi, K., Tomsia, A.P., Saiz, E., 2000. Characterization of Mo–SiO_2 functionally graded materials. Metell. Mater. Trans. A 31 (1), 299–308.

Ju, J.W., Chen, T.M., 1994. Effective elastic moduli of two-phase composites containing randomly dispersed spherical inhomogeneities. Acta Mech. 103 (1–4), 123–144.

Karlsson, A.M., Hutchinson, J.W., Evans, A.G., 2002. A fundamental model of cyclic instabilities in thermal barrier systems. J. Mech. Phy. Solids 50 (8), 1565–1589.

Kerner, E.H., 1956. The elastic and thermo-elastic properties of composite media. Proc. Phys. Soc. B 69 (8), 808–813.

Kesler, O., Matejicek, J., Sampath, S., Suresh, S., Gnaeupel-Herold, T., Brand, P.C., Prask, H.J., 1998. Measurement of residual stress in plasma-sprayed metallic, ceramic and composite coatings. Mater. Sci. Eng. A 257 (2), 215–224.

Khor, K.A., Gu, Y.W., 2000. Thermal properties of plasma-sprayed functionally graded thermal barrier coatings. Thin Solids Films 372 (1–2), 104–113.

Kim, J.H., Paulino, G.H., 2003. An accurate scheme for mixed-mode fracture analysis of functionally graded materials using the interaction integral and micromechanics models. Int. J. Numer. Meth. Eng. 58 (10), 1457–1497.

Kingery, W.D., Bowen, H.K., Uhlmann, D.R., 1976. Introduction to Ceramics, second ed. Wiley, New York.

Kondoh, J., Shiota, H., Kawachi, K., Nakatani, T., 2004. Yttria concentration dependence of tensile strength in yttria-stabilized zirconia. J. Alloys Compounds 365, 253–258.

Kröner, E., 1990. Modified Green functions in the theory of heterogeneous and/or anisotropic linearly elastic media. In: Weng, G.L., Taya, M., Abé, H. (Eds.), Micromechanics and inhomogeneity. Springer, New York, pp. 197–211.

Miyamoto, Y., Kaysser, W.A., Rabin, B.H., Kawasaki, A., Ford, R.G., 1999. Functionally graded materials: design, processing and applications. Kluwer Academic Publishers, Dordrecht.

Moon, R.J., Tilbrook, M., Hoffman, M., Neubrand, A., 2005. Al–Al_2O_3 Composites with interpenetrating network structures: composite modulus estimation. J. Am. Ceram. Soc. 88 (3), 666–674.

Mori, T., Tanaka, K., 1973. Average stress in matrix and average elastic energy of materials with misfitting inclusions. Acta Metall. 21 (5), 571–574.

Moschovidis, Z.A., Mura, T., 1975. Two-ellipsoidal inhomogeneities by the equivalent inclusion method. ASME J. Appl. Mech. 42 (4), 847–852.

Mura, T., 1987. Micromechanics of defects in solids, second ed. Kluwer Academic Publishers, Dordrecht.

Nemat-Nasser, S., Hori, M., 1999. Micromechanics: overall properties of heterogeneous materials, second ed. North-Holland, Amsterdam.

Neubrand, A., Chung, T.-J., Rödel, Steffler, E.D., Fett, T., 2002. Residual stress in functionally graded plates. J. Mater. Res. 17 (11), 2912–2920.

Paulino, G.H., 2004. Modeling of functionally graded materials, Int. J. Comput. Eng. Sci. 5 (4) (Special Issue).

Paulino, G.H., Jin, Z.H., Dodds, R.H., 2003. Failure of functionally graded materials. In: Comprehensive Structural Integrity, vol. 2, Elsevier Science Publisher, Amsterdam, pp. 607–644.

Paulino, G.H., Yin, H.M., Sun, L.Z., 2006. Micromechanics-based interfacial debonding model for functionally graded materials with particle interactions. Int. J. Damage Mech. (in press).

Percus, J.K., Yevick, G.J., 1958. Analysis of classical statistical mechanics by means of collective coordinates. Phys. Rev. 110 (1), 1–13.

Portinha, A., Teixeira, V., Carneiro, J., Beghi, M.G., Bottani, C.E., Franco, N., Vassend, R., Stoever, D., Sequeira, A.D., 2004. Residual stresses and elastic modulus of thermal barrier coatings graded in porosity. Surf. Coat. Technol. 188–189, 120–128.

Rangaraj, S., Kokini, K., 2003. Estimating the fracture resistance of functionally graded thermal barrier coatings fromtherm al shock tests. Surf. Coat. Technol. 173, 201–212.

Reiter, T., Dvorak, G.J., 1998. Micromechanical models for graded composite materials: II. thermomechanical loading. J. Mech. Phys. Solids 46 (9), 1655–1673.

Schulz, U., Peters, M., Bach, Fr.-W., Tegeder, G., 2003. Graded coatings for thermal, wear and corrosion barriers. Mater. Sci. Eng. A 362 (1–2), 61–80.

Suresh, S., Mortensen, A., 1998. Fundamentals of functionally graded materials. IOM Communications Ltd., London.

Teixeira, V., 2001. Numerical analysis of the influence of coating porosity and substrate elastic properties on the residual stresses in high temperature graded coatings. Surf. Coat. Technol. 146–147, 79–84.

Teixeira, V., Andritschky, M., Fischer, W., Buchkremer, H.P., Stöver, D., 1999. Effects of deposition temperature and thermal cycling on residual stress state in zirconia-based thermal barrier coatings. Surf. Coat. Technol. 120–121, 103–111.

Torquato, S., 2002. Random Heterogeneous Materials: Microstructure and Macroscopic Properties. Springer, New York.

Tsang, L., Kong, J.A., Ding, K.H., Ao, C.O., 2001. Scattering of Electromagnetic Waves, Numerical Simulations. Wiley, New York.

Tsukamoto, H., 2003. Analytical method of inelastic thermal stresses in a functionally graded material plate by a combination of micro- and macromechanical approaches. Compos. B. 34 (6), 561–568.

Vel, S.S., Batra, R.C., 2003. Three-dimensional analysis of transient thermal stresses in functionally graded plates. Int. J. Solids Struct. 40 (25), 7181–7196.

Wong, C.P., Bollampally, R.S., 1999. Thermal conductivity, elastic modulus, and coefficient of thermal expansion of polymer composites filled with ceramic particles for electronic packaging. J. App. Polym. Sci. 74 (14), 3396–3403.

Yin, H.M., Sun, L.Z., Paulino, G.H., 2004. Micromechanics-based elastic modeling for functionally graded materials with particle interactions. Acta Mater. 52 (12), 3535–3543.

Yin, H.M., Paulino, G.H., Buttlar, W.G., Sun, L.Z., 2005. Effective thermal conductivity of functionally graded particulate composites. J. App. Phys. 98 (6), 063704.

Zuiker, J.R., Dvorak, G.J., 1994. The effective properties of functionally graded composites—I. Extension of the Mori–Tanaka method to linearly varying fields. Compos. Eng. 4 (1), 19–35.